Research article

Deep insights into the optoelectronic properties of AgCdF$_3$-based perovskite solar cell using the combination of DFT and SCAPS-1D simulation

Fatema-Tuz- Zahra [a], Md Mehidi Hasan [a], Md. Bokhtiar Hossen [a], Md. Rasidul Islam [b,*]

[a] *Department of Materials Science and Engineering, Khulna University of Engineering & Technology (KUET), Khulna 9203, Bangladesh*
[b] *Department of Electrical and Electronic Engineering, Bangamata Sheikh Fojilatunnesa Mujib Science & Technology University, Jamalpur 2012, Bangladesh*

A R T I C L E   I N F O

Keywords:
DFT
AgCdF$_3$
SCAPS
Solar cell
Optoelectronic properties

A B S T R A C T

The main focus of this research is to explore the properties and photovoltaic application of AgCdF$_3$, and hence, initially, the CASTEP software was used in this study to assess the structural, optical, mechanical, and electrical characteristics of the AgCdF$_3$ perovskite absorber layer within the context of the density functional theory (DFT) method. AgCdF$_3$ resulting from the structural research is confirmed to be chemically and thermodynamically stable by the estimated tolerance factor and formation enthalpy. According to the band structure analysis, AgCdF$_3$ is an indirect band gap semiconductor with a band gap of 1.106 eV, where the electrons of Cd-4d and F-2s dominate the band edges of this semiconductor. Analysis of mechanical properties revealed that the AgCdF$_3$ cubic perovskite has a stable structure and enhanced ductility, indicating superior machinability. After completing the DFT analysis, a one-dimensional solar cell capacitance simulator 1D (SCAPS-1D) was used with three popular electron transport layers (ETLs), including ZnO, PCBM, and C$_{60}$, to examine the photovoltaic (PV) performance of various AgCdF$_3$-based solar cell heterostructures. Based on simulation findings, the device design with ITO/ZnO/ AgCdF$_3$/CuI/Au showed the highest photoconversion efficiency compared to the other configurations. A detailed analysis was conducted for the aforementioned configurations to determine the impact of variations in the absorber and ETL thickness on PV performance. Moreover, the effects of the three designs were assessed in terms of function, generation and recombination rate, capacitance, operating temperature, series and shunt resistance, and Mott-Schottky. Thus, this comprehensive simulation with validation results demonstrated the true potential of AgCdF$_3$ absorber with appropriate ETLs such as ZnO, PCBM, and C$_{60}$; on the other hand, the CuI as hole transport layer (HTL), paving the way for promising studies to develop high-efficiency AgCdF$_3$ PSCs for the photovoltaic industry.

1. Introduction

The exclusive reliance on traditional fossil fuels as the sole energy source for achieving sustainable development is no longer viable

---

* Corresponding author.
E-mail address: rasidul@bsfmstu.ac.bd (Md.R. Islam).

due to the increasing global energy demand and the detrimental impact on the environment [1–5]. Maximizing the utilization of solar energy and developing stable and efficient solar cells are crucial in addressing the worldwide energy crisis [6]. Among other solar cells, perovskite solar cells (PSCs) have shown a remarkable increase in efficiency from a pitiful 3.8–26.1 % in just ten years, which has attracted an unprecedented amount of research attention in order to cope with the present expansion of solar technology [7–9]. The significant progress achieved can be attributed to the exceptional optoelectronic properties exhibited by halide perovskite materials. These properties include a high absorption coefficient, variable band gaps, long-range charge diffusion lengths, low exciton binding energies, and high charge carrier mobilities [2,3,5,10,11]. All of the top-performing cells with power conversion efficiency (PCE) values of more than 20 % use perovskite absorbers with hybrid organic–inorganic compositions that use formamidinium (FA) or methylammonium (MA) as cations [12]. However, due to the inherent instability of the organic hybrid perovskites, such high power conversion efficiencies are not necessarily consistent with the longevity of the device [13]. Specifically, the organic components of the hybrid perovskites limit their thermal stability to less than 150 °C [12,14]. So, further investigation was necessary to determine thermally stable, cost-effective, and high-performance solar cells. Owing to that concern, the complex fluoride perovskites having general formula ABF_3 (A and B are cations while F is monovalent fluorine anion) are found to possess many unique characteristics such as high-temperature superconductivity [15], colossal magneto resistivity [16], optical property [17–19], thermoelectricity [20], and photoluminescence [21] among all the perovskites.

In recent times, DFT approaches have become very popular to explore the geometrical, optical, mechanical, and electrical properties of such types of fluoroperovskite materials as well as to determine its suitability for PV applications [22–24]. Hussain et al. computed the mechanical, magnetic, and thermoelectric behavior of perovskite oxides $XGaO_3$ (X = Sc, Ti, Ag) using LDA + U functional, which reveals the half-metallic nature of the compounds supporting their applications in spintronics [25]. Various properties of silver-based perovskites $AgXCl_3$ (X = Ca, Sr) are investigated by using the FPLAPW method within the wien2k code [26]. Electronic property analysis of that study reveals a band gap of 1.44 and 1.37 eV for $AgCaCl_3$ and $AgSrCl_3$, respectively, whereas the mechanical property demonstrates the ductile nature of the two compounds. The first principle calculations of $AgMO_3$ (M = V, Nb, and Ta) show that $AgNbO_3$ and $AgTaO_3$ are indirect bandgap materials while $AgVO_3$ is metallic [27]. In recent research, Singh et al. investigated the thermoelectric performance of $AgMF_3$ (M = Zn, Cd), where the electronic properties and the transport coefficients are obtained by using the density functional theory combined with the Boltzmann transport theory under relaxation time approximation [28]. In this study, the band structures and thermoelectric properties of $AgZnF_3$ and $AgCdF_3$ have been focused on, but to the best of our knowledge, no other characteristics have been conducted yet. Hence, in order to assess the viability of employing $AgCdF_3$ as a prospective absorber material for solar cells, a comprehensive analysis of its structural, optical, mechanical, and electrical characteristics will be conducted. This investigation will be carried out through the utilization of DFT calculations inside the Cambridge Serial Total Energy Package (CASTEP) software framework.

Additionally, to explore the performance of $AgCdF_3$ perovskite in solar cells, it is essential to have a comprehensive understanding of how the various constituent layers in PSCs—transparent conductive oxide (TCO), perovskite absorber layer (PAL), ETL, HTL, and back-metal contact layer—affect the solar cell (SC) performance [29–31]. One important aspect impacting PV characteristics is the optical absorption attributes of PAL. The ETL and HTL are required to transport and extract the charge carriers generated during photon absorption in the PAL. The difference in Fermi energy levels between the HTL and ETL controls the open circuit voltage (V_{OC}) [32]. On the other hand, the fill factor (FF) and short circuit current density (J_{SC}) increase in proportion to the increased charge mobility of ETL [33–35]. In solar cells, ETL and HTL are made of both organic and inorganic components. A number of common ETLs, like ZnO [36,37], C_{60} [32], and PCBM [38], are used with CuI [39] as HTL because of their suitable band gap, band alignment, charge mobility, and transparency. Another important parameter to consider while examining the performance of PSCs is the choice of work function of back contact material [40,41].

Therefore, the specific aim of this study is to investigate the structural, electronic, optical, and mechanical characteristics of $AgCdF_3$ cubic perovskite using DFT. In addition, three feasible designs have been thoroughly examined to verify the viability of $AgCdF_3$ as an absorber layer in perovskite solar cells. The impact of absorber layer thickness, back contact work function, generation-recombination rate, series and shunt resistance, Mott-Schottky, and temperature on the PV parameters of these three configurations have been investigated through SCAPS-1D simulation.

2. Computational method

2.1. First-principle calculation of AgCdF₃ absorber layer

In this study, the Cambridge Serial Total Energy Package (CASTEP), which is based on density functional theory (DFT), is used to analyze the structural characteristics, electrical configurations, and optic response to electromagnetic radiation of $AgCdF_3$. First, the previously published experimental parameters are taken into consideration while drawing the $AgCdF_3$ structural model. The functional Perdew−Burke−Ernzerhof (PBE) is widely employed in conjunction with the exchange correlation of generalized gradient approximation (GGA) to produce the ground-state structure (optimal structure) [42,43]. Utilizing Ag: 4 d^{10} 5s^1, Cd: 4 d^{10} 5s^2, and F: 2s^2 2p^5 as valance electrons, pseudoatomic computations were carried out. Plane-wave basis sets and pseudopotential as core-valence states interaction are selected for computations. In order to produce interactions between electrons and ions, the most widely used Vanderbilt-type ultrasoft pseudopotential is treated [44]. During structural optimization, the Broyden-Fletcher-Goldfarb-Shanno (BFGS) algorithm has been used. While the optimization technique employs a range of cutoff energies, 700 eV has been found to be compatible with it. Furthermore, in order to facilitate improved optimization, a 12 × 12 × 12 k-point mesh fitted with the Monkhorst-Pack technique is fitted to sample the Brillouin zone. Over the first Brillouin zone, the sampling integration is set to

ultrafine quality. The selected optimum converging functions of total energy, maximum ionic force, maximum ionic displacement, and maximum stress are 1×10^{-6} eV/atom, 5×10^{-4}, 0.01 GPa, 0.05 GPa, and 5×10^{-6} eV/atom, respectively. Following the optimization procedure, the relaxations of the lattice parameters and atomic locations are determined. By adjusting the same characteristics, such as structural optimization, the electronic and optical parameters are estimated. Kramers-Kronig relations use Eigen values and Eigen functions for optical qualities that are taken from density functional perturbation theory (DFPT) simulations. The CASTEP module utilizes the 'stress-strain' method for elastic constants and elastic moduli calculations.

2.2. SCAPS-1D numerical simulation

To model perovskite PSCs, the ELIS department at the University of Gent developed the SCAPS-1D code. With the help of realistic and accurate back-end physical equations, a wide range of device architectures can be designed and investigated using the flexible PV software SCAPS 1D. This software simulates photovoltaic processes like light absorption, exciton generation, charge transfer and collection, and recombination. Therefore, the solar cell and its associated features were modeled using SCAPS-1D. The SCAPS-1D model has a high level of concurrence with empirical observations. Equation (1) defines Poisson's equation, which defines the relation between electrostatic potential and the charge density. The relationship between the distribution of charge density and the electrostatic potential can be comprehended through the use of Poisson's equation [45–49]. Conversely, in order to ascertain the characteristics pertaining to the quality of a solar cell, the continuity formula for both electrons and holes is employed. Furthermore, the program incorporates Shockley-Read-Hall (SRH) recombination statistics in order to model the functioning of the device [50].

$$\frac{d^2}{dx^2}\Psi(x) = \frac{q}{\epsilon_0\epsilon_r}\left[p(x) - n(x) + N_D - N_A + \rho_p - \rho_n\right] \tag{1}$$

In this context, Ψ represents the electric potential, q denotes the electronic charge, ϵ_0 represents the permittivity in a vacuum, and ϵ_r refers to the relative permittivity. Additionally, N_A and N_D represent the density of acceptors and donors respectively. The variables p and n are used to denote the concentration of holes and electrons respectively. Lastly, ρ_p and ρ_n represent the holes and electrons charge density respectively.

$$\frac{\delta p}{\delta t} = \frac{1}{q}\frac{\delta J_p}{\delta x} + (G_p - R_p) \tag{2}$$

$$\frac{\delta n}{\delta t} = \frac{1}{q}\frac{\delta J_n}{\delta x} + (G_n - R_n) \tag{3}$$

The equations presented include the variables J_p and J_n, which represent the holes and electrons current density, respectively. Additionally, G_n and G_p represent the production rate of electrons and holes, respectively, while R_n and R_p denote the electrons and holes recombination rate, respectively. The SCAPS 1D software is capable of producing a steady-state response in one dimension, taking into account the specified equations and boundary conditions [51,52].

$$\text{Device efficiency}, \eta = \frac{V_{OC} \times J_{SC} \times FF}{P_{in}} \tag{4}$$

$$\text{Fill factor}, FF = \frac{J_{mp} \times V_{mp}}{J_{sc} \times V_{Oc}} \tag{5}$$

V_{mp} and J_{mp} represent the maximum voltage and current density, respectively. V_{OC} and J_{SC} are abbreviations that respectively denote open-circuit voltage and short-circuit current density.

3. Results and discussion

3.1. DFT results analysis

3.1.1. Structural properties

Together with the space group Pm-3m, the compound $AgCdF_3$ has a cubic structure. The fractional coordinates of Ag, Cd, and F are (0,0,0), (0.5,0.5,0.5), and (0,0.5,0.5), with the corresponding Wyckoff positions being 1a, 1b, and 3c. The lattice constants of $AgCdF_3$ are a = b = c = 4.34 Å, according to the results of the prior studies [28,53]. Fig. 4b presents the optimized crystal structure of $AgCdF_3$ as a structural model of $AgCdF_3$ in the present study. The lattice parameter of $AgCdF_3$ has become a = b = c = 4.373 Å resulting from geometrical optimization. The above scenario indicates a small increase in the lattice parameter (0.033 Å), indicating a 0.76 % divergence of the lattice parameters from the reference. Since the deviation is so small, we may assume that the accuracy of our first-principle calculations is adequate. Again, the stability of the compound can be accessed by the formation energy ($E_f = -4.49$ eV/atom) with equation. 6.

$$E_f(AgCdF_3) = \frac{\left[E_{total}(AgCdF_3) - aE_f(Ag) - bE_f(Cd) - cE_f(F)\right]}{a + b + c} \tag{6}$$

The optimized structure possesses a stable structural design suitability for the construction of the solar system, as evidenced by its substantial negative forming energy value.

3.1.2. Electronic properties

As illustrated in Fig. 1, the electronic band structure, density of states, and charge density of the AgCdF$_3$ perovskite are computed based on the optimized structure in order to investigate its electronic features. AgCdF$_3$ is clearly an indirect band gap semiconductor based on the band structure computed at high symmetry k-points in the Brillouin zone (Fig. 1). The computed band structure places the valence band maximum (VBM) at various k points in the Brillouin zone, while the conduction band minimum (CBM) is located at the G point. The measured band gap (E$_g$) is 1.106 eV, slightly higher than the 1.06 eV theoretically estimated E$_g$ value obtained in other publications [53]. The analysis of band structure formation can be accomplished by examining the density of states (DOS) plots illustrated in Fig. 2. The occupied and unoccupied energy states are clearly separated in the total density of states (TDOS) as shown in Fig. 2c, which lacks any electronic state overlap at the Fermi level. This means that TDOS also supports the band structure result by confirming that the material in question has a band gap at the Fermi level.

Analysis of the partial and orbital DOS of the component atoms can be used to investigate the atomic origin of the energy bands that exist within valence (conduction) bands. Ag atoms do not significantly contribute to the development of the band edges, as seen in Fig. 2a, and Ag 4d sites are found to be close to the Fermi level. However, Ag 4d valence electron states are primarily responsible for the observed high-intensity peak in Fig. 2a, which is located approximately −4 eV just below the Fermi level. Ag 4p states have a minor role, and 5s play no function in forming band edges. On the other hand, as Fig. 2(b and c) illustrates, the Cd 4d and F 2s states clearly contribute to the electrical states generating the band gap. Consequently, the band gap between the constituent Ag, Cd, and F atoms is generated by the hybridization between the electronic states of Cd and F atoms.

3.1.3. Optical properties

To uncover additional information about the optical characteristics of compounds, the complicated dielectric function is essential [54]. These characteristics make the materials of great significance while examining possible uses in solar and other optoelectronic devices. The nature of the six computed optical parameters—absorption, reflectivity, refractive index, conductivity, dielectric constants, and energy loss function is described in this paper in terms of energy up to 50 eV. Depending on the photon energy, determining the dielectric function is the initial step to derive other optical properties as well. Dielectric function is a complex equation that can be expressed as $\varepsilon(\omega) = \varepsilon_1(\omega) + i\varepsilon_2(\omega)$; here $\varepsilon_1(\omega)$, $\varepsilon_2(\omega)$ are the real and imaginary part of the dielectric function respectively. The real part can be calculated from the imaginary part by following the Kramers-Kronig dispersion equation as follows.

$$\varepsilon_1(\omega) = 1 + \frac{2}{\pi} P \int_0^\infty \frac{\omega'^{\varepsilon_2}(\omega')}{\omega'^2 - \omega^2} d\omega' \tag{7}$$

The imaginary part can be derived by momentum tensors element between the occupied and unoccupied wave function as follows.

$$\varepsilon_2(\omega) = \frac{2e^2\pi}{\Omega\varepsilon_0} \sum_{K,V,C} |\langle \psi_k^c | \widehat{U} \cdot \vec{r} | \psi_k^V \rangle|^2 \delta\left(E_K^C - E_K^V - E\right) \tag{8}$$

Here, ω stands for the frequency of light. ψ_k^c and ψ_k^V represents the conduction and valance band wave function at k, respectively.

Fig. 3a displays the real and imaginary components of the AgCdF$_3$ dielectric function. Since it depends significantly on the
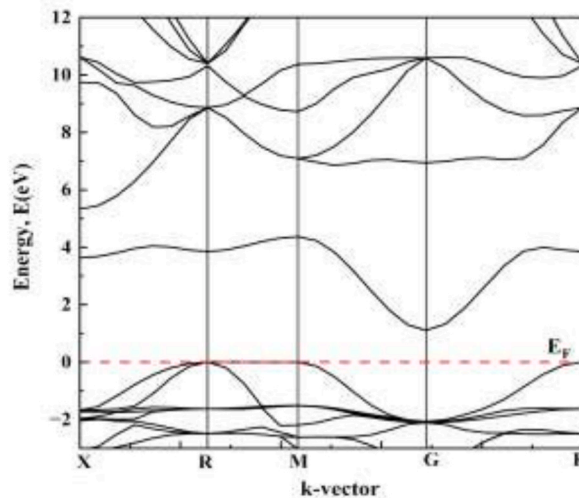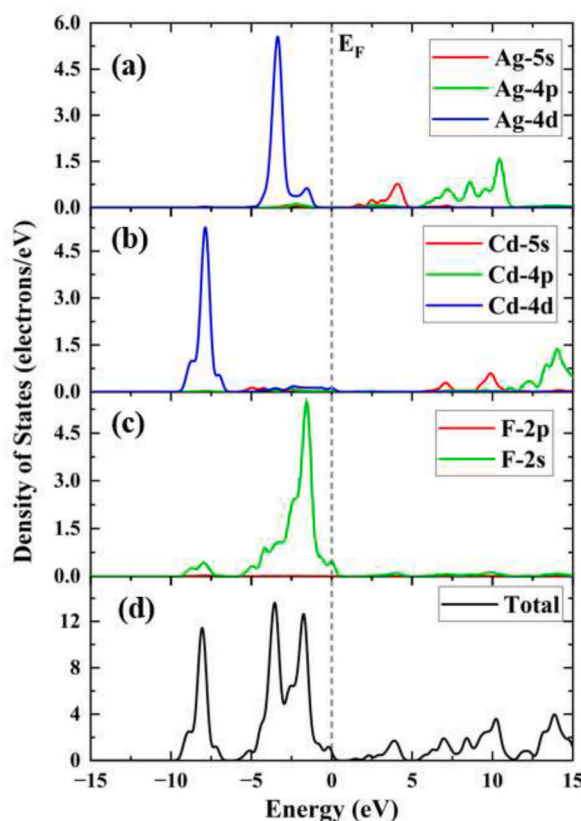

**Fig. 1.** The electronic energy band diagram of AgCdF$_3$ using GGA + PBE approximation.

Fig. 2. Orbital density of states representation of (a) Ag, (b) Cd, (c) F, and (d) total density of states of AgCdF$_3$ cubic perovskite using GGA + PBE functional.

compound's band gap, the most significant measurement of the real part of the dielectric function, $\varepsilon_1(\omega)$, is the zero-frequency limit, meaning the electronic component of the static dielectric constant, $\varepsilon 1(0)$. Compounds that achieve a broad energy bandgap typically exhibit a low peak dielectric constant value. There exists a correlation between the electronic polarizability of the compounds and the real part of the dielectric function. The static dielectric constant at 0 eV can be obtained from Fig. 3a as $\varepsilon_1(0) = 2.81$. $\varepsilon_1(\omega)$ exhibits its maximum value in the visible region of the electromagnetic spectrum, after which it commences a sharp decline towards zero. The relationship between photon absorption and the imaginary portion of the dielectric function $\varepsilon_2(\omega)$, which characterizes the electronic properties of crystalline materials, is established. The abrupt peaks observed in the $\varepsilon_2(\omega)$ represent the transition of charge carriers from occupied to vacant bands. The compound AgCdF$_3$ demonstrates noteworthy values of $\varepsilon_2(\omega)$ within the range of 0–12 eV. This suggests that it may serve as a reasonable choice for optoelectronic purposes in the visible and ultraviolet regions.

One important physical factor that describes a material's optical properties is its refractive index (n). In a given medium, the phase velocity of electromagnetic (em) waves is correlated with the refractive index [55]. The refractive index, as shown in Fig. 3b, closely resembles the dielectric function when it is obtained from $\varepsilon(\omega)$. In the visible portion of the electromagnetic spectrum, the compound AgCdF$_3$ has a strong peak at about 3.2 eV, and its predicted static refractive index, or n(0), is around 1.65. It moves further, although at lower energy, into the ultra-violet (UV) regions. Predicting the suitability of AgCdF$_3$ perovskite material for solar cell applications requires careful consideration of this information.

The energy-dependent reflectance spectrum is a crucial optical function that is used to calculate all optical coefficients utilizing Kramers-Kroning relationships. Reflectance spectrum (R) is also highly important for AgCdF$_3$ utilization as a solar absorber material. At zero frequency, reflectivity begins at about 0.06. After that, R increases quickly until it reaches its maximum value of 0.1 at around 3.5 eV of photon energy. Interband transitions may have contributed to the maximum degree of reflection in the UV area shown in Fig. 3c. Furthermore, three distinct steep peaks outside of the visible and ultraviolet regions can be observed at energies of 12.14, 22.6, and 26.5 eV. The maximal reflectance of AgCdF$_3$ (0.13) is still very low compared to other perovskite materials generally used as an absorber layer in solar cell applications.

The optical conductivity σ (ω) of a medium indicates its ability to initiate a conduction process. The complex dielectric function can be used to compute it [54]. The curve shown in Fig. 3e makes it clear that conductivity increases as energy increases up to around 12 eV. After that, conductivity declines with a brief oscillatory phase, climbs again at about 21.7 eV, and finally becomes static. As seen in Fig. 3d, σ(ω) is increasing in the visible and ultraviolet regions due to the increasing absorption coefficient in this energy range. The loss spectrum (L) of AgCdF$_3$ (Fig. 3f) illustrates the energy a fast electron loses as it passes through a compound. The electron-matter
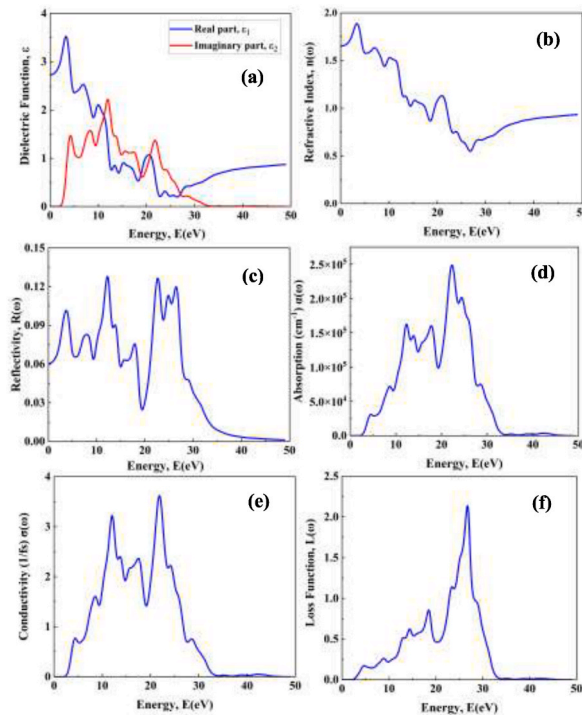
Fig. 3. Six optical functions computed for the AgCdF$_3$ perovskite solar absorber: (a) dielectric function, (b) refractive index, (c) reflectivity, (d) absorption, (e) conductivity, and (f) loss function.

interaction-induced energy loss in electrons is the only phenomenon explained by the energy loss function [54]. It is evident that energy loss grew steadily, peaking at 18.5 eV for photon energy, with a few smaller peaks in between. After that, it rapidly picked up speed, reaching its plasma frequency (p), or peak energy loss (2.1), at around 26.7 eV. Since photon energy is higher than band gap energy, it is evident that most energy loss takes place in the ultraviolet band.

3.1.4. Mechanical properties

This section provides a comprehensive analysis of the elastic constants and other significant mechanical characteristics to assess the mechanical stability of AgCdF$_3$. The elastic constants and Cauchy pressure (C$_{12}$–C$_{44}$) of the compound have been compiled and presented in Table 1.AgCdF$_3$ exhibits a limited number of independent elastic constants (C$_{11}$, C$_{12}$, and C$_{44}$) when the stress-strain matrix is analyzed using Hooke's Law in conjunction with the lattice dynamics and considering the lattice symmetry. All of the elastic constants clearly meet the well-established Born stability criterion, which specifies that [56]-

C$_{11}$ > 0, C$_{44}$ > 0, C$_{11}$–C$_{12}$ > 0, and C$_{11}$ + 2C$_{12}$ > 0

Therefore, the compound exhibits mechanical stability. The characterization of material brittleness and ductility can be achieved through the utilization of the Cauchy pressure, denoted as C$_{12}$–C$_{44}$. The Cauchy pressure, when positive (negative), serves as an indicator of the material's ductile (brittle) characteristics. The positive values obtained for this metric indicate that the sample exhibits sufficient ductility. The mechanical characteristics, including the bulk modulus B, shear modulus G, Young's modulus E, Poisson's ratio υ, Pugh's ratio B/G, and Vicker's hardness (HV), are derived and organized in a table based on the evaluated elastic constants C$_{ij}$. The well-accepted Voigt-Reuss approach was employed to ascertain the values of the bulk modulus B and shear modulus G [57]. The upper and lower bounds of the actual effective modulus correspond to the Voigt and Reuss bounds obtained from the typical polycrystalline modulus under two assumptions, respectively: uniform strain and uniform stress in a polycrystal. For cubic lattices, Voigt bulk modulus (B$_V$) and shear modulus (G$_V$) are [57]:

$$B_V = \frac{1}{3}(C_{11} + 2C_{12}) \tag{9}$$

Table 1
The evaluated elastic constants C$_{ij}$ (GPa) and Cauchy pressure C$_{12}$–C$_{44}$ (GPa) of AgCdF$_3$.

Compound	C$_{11}$	C$_{12}$	C$_{44}$	C$_{12}$–C$_{44}$
AgCdF$_3$	102.92	23.24	4.81	18.43

$$G_V = \frac{1}{5}(C_{11} - C_{12} + 3C_{44}) \tag{10}$$

Again, for cubic lattices, Reuss bulk modulus (B_R) and Reuss shear modulus (G_R) are:

$$B_R = B_V = \frac{1}{3}(C_{11} + 2C_{12}) \tag{11}$$

$$G_R = \frac{5C_{44}(C_{11} - C_{12})}{[4C_{44} + 3(C_{11} - C_{12})]} \tag{12}$$

According to Hill's theory, the practical estimate of the bulk and shear modulus is the arithmetic mean of the two values of the Voigt and Reuss equations. Consequently, the practical estimated value (Hill's average) for the bulk modulus (B_H) and shear modulus (G_H) is given by:

$$B_H = \frac{1}{2}(B_v + B_R) \tag{13}$$

$$G_H = \frac{1}{2}(G_v + G_R) \tag{14}$$

Besides, Young's modulus (E), Poisson's ratio (υ), Vicker's hardness (H_V), and machinability index (μ_M) are given by Refs. [58,59]:

$$E = \frac{9BG}{3B + G} \tag{15}$$

$$\upsilon = \frac{3B - E}{6B} \tag{16}$$

$$H_V = \frac{(1 - 2\upsilon)E}{6(1 + \upsilon)} \tag{17}$$

$$\mu_M = \frac{B}{C_{44}} \tag{18}$$

The resistance to fracture can be quantified by the bulk modulus B, while the resistance to plastic deformation can be quantified by the shear modulus G [60]. Hence, it can be surmised that the resistance of AgCdF$_3$ to fracture can be attributed to its higher bulk modulus. The rigidity of AgCdF$_3$ can be derived from the shear modulus G. Furthermore, the stiffness of the material can be characterized by Young's modulus, denoted as E. Frantsevich and Pugh (year) have established that a Poisson's ratio value of 0.26 is crucial in distinguishing between ductility and brittleness [60]. To attain ductility, the Poisson's ratio, $\ddot{U}$, is required to be higher than the critical value. According to the data presented in Table 2, the values of υ suggest that the compound exhibits sufficient ductility. In addition, the relationship between the ductility and brittleness of a material can be elucidated by the utilization of Pugh's ratio (B/G). Based on Pugh's relationship, it may be concluded that a larger ratio value may be indicative of the ductility exhibited by a material. Likewise, the lower magnitude of the ratio is linked to the characteristic of brittleness exhibited by a substance. The Pugh's ratio exhibits a crucial value of 1.75, which demonstrates variation across these two distinct properties. The material exhibits ductility when the ratio of its bulk modulus (B) to its shear modulus (G) exceeds 1.75. Therefore, based on the data presented in Table 2, it may be concluded that the material exhibits ductility. To understand the elastic and plastic properties of a material hardness measurement is important. From Table 2, the hardness of the compound is found to be only 1.05 GPa. So, the compound is soft and can be dented easily. The machinability index is the measurement of the plasticity and lubricating nature of a material. Good lubricating properties, low feed friction, and a higher plastic strain value correlate with a higher value of the machinability index [61]. So, according to the value μ_M, AgCdF$_3$ is good in these characteristics.

3.2. Analysis of SCAPS-1D simulation results

3.2.1. AgCdF$_3$ perovskite solar cell structure

The functionality of AgCdF$_3$-based SC can be enhanced by integrating the perovskite AgCdF$_3$ absorber layer (800 nm) with a band gap of 1.106 eV and suitable substitutes for traditional HTL, ETL, and back contact materials. We conducted a computational analysis and evaluated the suitability of various ETLs in this work by choosing three different heterostructures in the SCAPS-1D to develop a

Table 2
Calculated bulk modulus, B (GPa), shear modulus, G (GPa), Young's modulus, E (GPa), Poisson's ratio, υ, Pugh's ratio (B/G) and Vicker's hardness, H_V (GPa) and machinability index (μ_M) of AgCdF$_3$.

Compound	B_V	B_R	B_H	G_V	G_R	G_H	E	υ	B/G	H_V	μ_M
AgCdF$_3$	49.8	49.8	49.8	18.82	7.42	13.12	36.18	0.38	3.8	1.05	10.35

heterostructure combination that would minimize the time and expense complexity required to build such a large number of SC configurations physically. These factors have led to the analysis of three different ITO/ETL/AgCdF$_3$/CuI/back contact heterostructure combinations for AgCdF$_3$-based PV configurations using ETL like PCBM (50 nm), ZnO (50 nm), and C$_{60}$ (50 nm) (Fig. 4a) in conjunction with Ag, Fe, Nb, Cu-graphite alloy, and Au as distinct back contact materials. We also explored how the AgCdF$_3$ absorber and ETL thickness affected the PV parameter performance of the three configurations. Furthermore, the effects of generation, recombination rate, Mott-Schottky (MS), capacitance, operating temperature, and series and shunt resistance were assessed.

The simulation parameters for each layer, including the TCO, ETL, Absorber, & HTL, are shown in Tables 3 and 4. For the simulation, the selected conditions were AM1.5G solar spectrum with a power density of 100 mW/cm^2 at a temperature of 300 K. The respective values for the acceptor concentration and defect densities are set at 10^{18} cm^{-3} and 10^{15} cm^{-3}. The following sections cover research conducted to explore the device configurations listed in Table 4.

3.2.2. Energy band diagram (EBD) of AgCdF$_3$

In order to enhance the efficiency of AgCdF$_3$-based PSCs, simulations were conducted to investigate the impact of ETLs with varying optoelectronic characteristics. Each ETL had an impact on the EBD.

The disparity in energy levels notably influences the performance and efficiency of PSCs. The electrons created during the process of photoexcitation are incidented into ETL, where they are then transported to HTL by holes. Subsequently, the accumulation of electrons and holes takes place at the front contact metal (ITO) and rear contact metal (Au), respectively. In order to facilitate the extraction of electrons at the interface between the ETL and AgCdF$_3$, it is necessary for the electron affinity of AgCdF$_3$ to be comparatively lower than that of each ETL component, namely ZnO, PCBM, and C$_{60}$ [38]. In order to extract the holes at the interface between AgCdF$_3$ and CuI HTL, it is necessary for the ionization energy of AgCdF$_3$ to exceed that of CuI HTL. Furthermore, the disparity in energy bands at the interfaces significantly affects the device's performance, including J$_{SC}$, V$_{OC}$, FF, and PCE parameters.

The relationship between the creation of two structures is associated with the conduction band offset (CBO). When the CBO exhibits a negative value, the energy difference has a cliff-like profile [65], while a positive CBO results in an energy difference resembling a spike (Fig. 5). The concept of negative charge carrier, specifically in the context of the CBO phenomenon, pertains to the efficient movement of electrons. The absorber exhibits a higher conduction band than the ETL, leading to a negative CBO and the absence of a potential barrier for electrons at the interface between the ETL and absorber. However, when the conduction band of the absorber is lower than that of the ETL, it leads to a positive CBO with a potential barrier for electrons at the interface between the ETL and absorber. The presence of this potential barrier facilitates the accumulation of electrons in close proximity to the interface between the ETL and the absorber material. Consequently, this accumulation increases recombination when the electrons are transferred back to the interface of the heterojunction. On the contrary, the presence of positive charge carriers in the CBO results in a phenomenon known as band bending, which subsequently reduces recombination processes. From Fig. 5, it is observed that CBO is positive and shows a spike nature for all the three ETLs. Among them, ZnO shows less spike than the other two facilitating less recombination rate and higher efficiency.

However, it is essential for the VBM of the absorber to be higher than that of the HTL in order to facilitate efficient hole transport. The activation energy (E$_a$) associated with the process of recombination may be determined by subtracting the band gap energy (E$_g$) from the ratio of the CBO and VBO [66]. There exists an inverse relationship between activation energy and recombination. In Fig. 5 (a–c), it can be shown that the VBO exhibits a sufficiently modest magnitude, hence facilitating effective hole transport at the interface between the HTL and the perovskite material. The transit of holes from the absorber layer to the conductive electrode is facilitated by the HTL. Hence, the composition and quality of the HTL significantly influence the overall performance of the solar cell, including V$_{OC}$ and J$_{SC}$. The current density enhancement is achieved by mitigating electron-hole recombination at the interface between the absorber and HTL. This task may be accomplished by using a high-quality HTL implementation. The highest PCE of 27.12 % was achieved with the configuration of ITO/ZnO/AgCdF$_3$/CuI/Au. Additionally, other ETLs have comparable PCEs of 27.04 % and 25.64 % for PCBM and C$_{60}$, respectively.
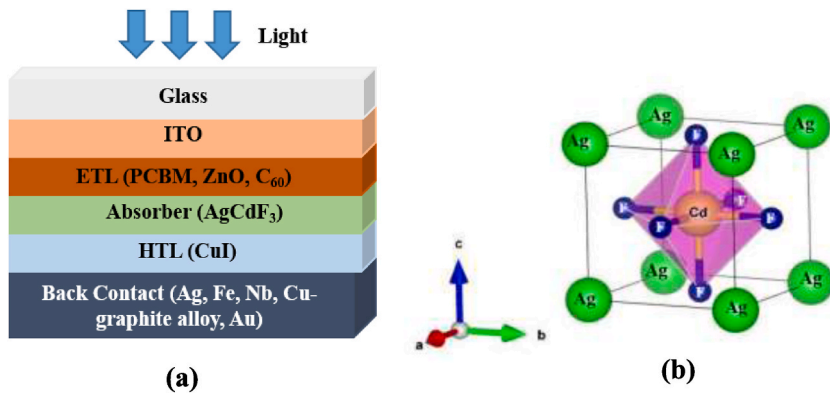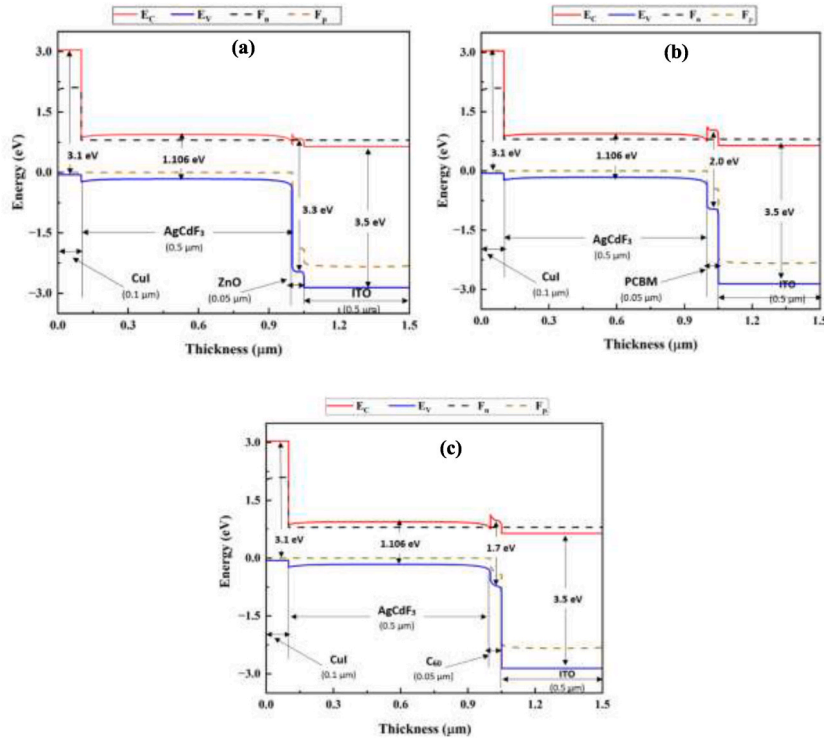

Fig. 4. (a) Design of AgCdF$_3$-based perovskite solar cell, and (b) An optimized primitive unit cell of AgCdF$_3$ where the Cd-atom is located at an octahedral site surrounded by six fluorine atoms.

Table 3

Input parameters of TCO, ETL, and absorber layer (AgCdF$_3$).

| Parameters	ITO (TCO)	PCBM (ETL)	ZnO (ETL)	C$_{60}$ (ETL)	CuI (HTL)	AgCdF$_3$
Thickness (nm)	500	50	50	50	100	800
Band gap, E$_g$(eV)	3.5	2	3.3	1.7	3.1	1.106
Electron affinity, (eV)	4	3.9	4	3.9	2.1	4.27
Dielectric permittivity (relative)	9	3.9	9	4.2	6.5	2.81
CB effective density of states	2.2×10^{18}	2.5×10^{21}	3.7×10^{18}	8.0×10^{19}	2.8×10^{19}	1.107×10^{17}
VB effective density of states	1.8×10^{19}	2.5×10^{21}	1.8×10^{19}	8×10^{19}	1×10^{19}	2.3×10^{17}
Electron mobility (cm^2/Vs)	20	0.2	100	8×10^{-2}	100	831
Hole mobility (cm^2/Vs)	10	0.2	25	3.5×10^{-3}	43.9	54
Shallow uniform acceptor density	0	0	0	0	1.0×10^{18}	8.36×10^7
Shallow uniform donor density	1×10^{21}	2.93×10^{17}	1×10^{18}	1×10^{17}	0	0

Table 4

Optimized PV parameters of the AgCdF$_3$-based solar cell for CuI HTL with Au back contact and different ETLs (ZnO, PCBM, C$_{60}$).

Optimized device configuration	V$_{oc}$ (V)	J$_{sc}$ (mA/cm^2)	FF (%)	PCE (%)
ITO/ZnO/AgCdF$_3$/CuI/Au	0.823	42.472	77.62	27.12
ITO/PCBM/AgCdF$_3$/CuI/Au	0.823	42.435	77.47	27.04
ITO/C$_{60}$/AgCdF$_3$/CuI/Au	0.822	41.613	74.96	25.64

Fig. 5. Energy band diagram of AgCdF$_3$-based perovskite solar cell with CuI HTL, Au back contact, and different ETLs: (a) ZnO, (b) PCBM, and (c) C$_{60}$.

3.2.3. Effect of absorber thickness and work function on PV performance

Fig. 6 depicts the influence of the work function of the back contact material shown in Table 5 and the thickness of the absorber layer on the behavior of V$_{OC}$. All of the contour plots in Fig. 6 show a general trend of decreasing V$_{OC}$ with increasing thickness of the absorber layer. In Fig. 6, it is seen for ETL ZnO that with the max V$_{OC}$ of 0.8536 V is shown for a thickness of ~0.5 μm and work function of (4.9–5.1) eV. With the decrease of back contact work function and an increase in absorber thickness, the V$_{OC}$ decreases. V$_{OC}$ can be defined by the following equation –
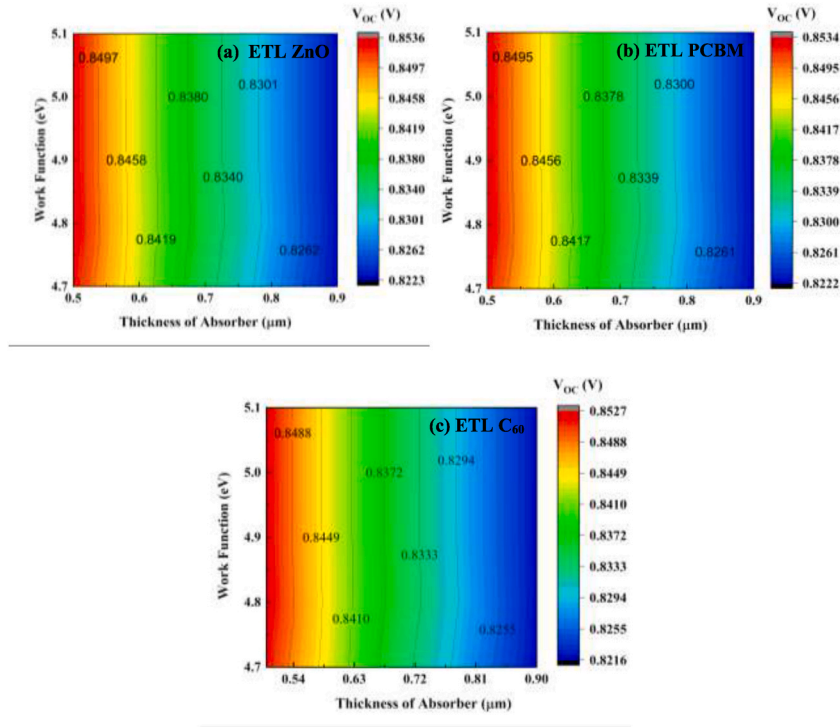
Fig. 6. Contour plots illustrating the variation in V_{OC} for $AgCdF_3$-based SC when (a) ZnO, (b) PCBM, and (c) C_{60} ETLs were incorporated, in addition to the concurrent changes in absorber layer thickness and work function.

Table 5
Different materials exhibiting the simulated work functions [62–64].

Material	Ag	Fe	Nb	Cu-graphite alloy	Au
Work function (eV)	4.7	4.8	4.9	5.0	5.1

$$V_{OC} = \frac{nkT}{q} \ln\left(\frac{I_L}{I_O} + 1\right) \qquad (19)$$

Here, n is a factor, kT/q is thermal voltage, I_L is light-generated current, and I_O is dark saturation current. An increase of V_{OC} indicates electron-hole recombination is lower at a thinner thickness of absorber and value of I_O is at low level. Hence, increase of excess carrier concentration generate higher I_L which increases the value of V_{OC} according to Eq. (19). However, as the thickness of the absorber increases, it increases the value of I_O and promotes carrier recombination which decreases the value of V_{OC}. In Fig. 6b for PCBM, the maximum V_{OC} is 0.8534 V, which is quite similar to ZnO. The maximum V_{OC} for PCBM also occurs at a thickness of ~0.5 μm and a work function of (4.9–5.1) eV. Similarly, in Fig. 6c ETL C_{60} shows a similar behavior to the other two ETLs. C_{60} shows a maximum V_{OC} of 0.8527 V, at a thickness of ~0.5 μm, and a work function of (4.9–5.1) eV. Among all 3 ETLs, ZnO shows the maximum V_{OC} given all other parameters remain the same.

The influence of absorber thickness and metal work function of back contact on the J_{SC} characteristics is represented in Fig. 7 where it is clearly seen that metal work function has no effect on the J_{SC} characteristics of the PSC. Although J_{SC} characteristics are independent of metal work function, significant change occurs due to changes in absorber thickness. It is seen from Fig. 7 that as the absorber thickness increases, the J_{SC} value increases. The maximum J_{SC} value of 42.48 mA/cm² is seen for ETL ZnO at a thickness greater than 0.85 μm. PCBM also shows a similar value of 42.47 mA/cm² for J_{SC}, which also appears at a thickness greater than 0.85 μm. As the absorber thickness increases, it causes more light absorption along with increase of excess carrier concentration which elevates the value of J_{SC}. The lowest J_{SC} value of 41.62 mA/cm² is shown by C_{60} at a thickness greater than 0.85 μm. Fig. 8 represents the contour plot of the fill factor, showing the influence of back contact metal work function and absorber thickness. FF determines the ability to deliver available power to a load generated by a cell or the internal power depletion. For SCs, higher FF is desirable for better performance. All three ETLs show similar behavior in terms of FF. In Fig. 8, ETL ZnO shows a maximum of 79.95 % FF for absorber thickness in the range between (0.5–0.6) micrometer and work function in the range(4.9–5.1) eV. PCBM also shows the same behavior with a maximum of 79.80 % FF in Fig. 8b for absorber thickness in the range between (0.5–0.6) micrometer and work function in the range (4.9–5.1) eV. ETL C_{60} shows a slight decrease in FF with a maximum value of 79.50 % and the same range for absorber thickness
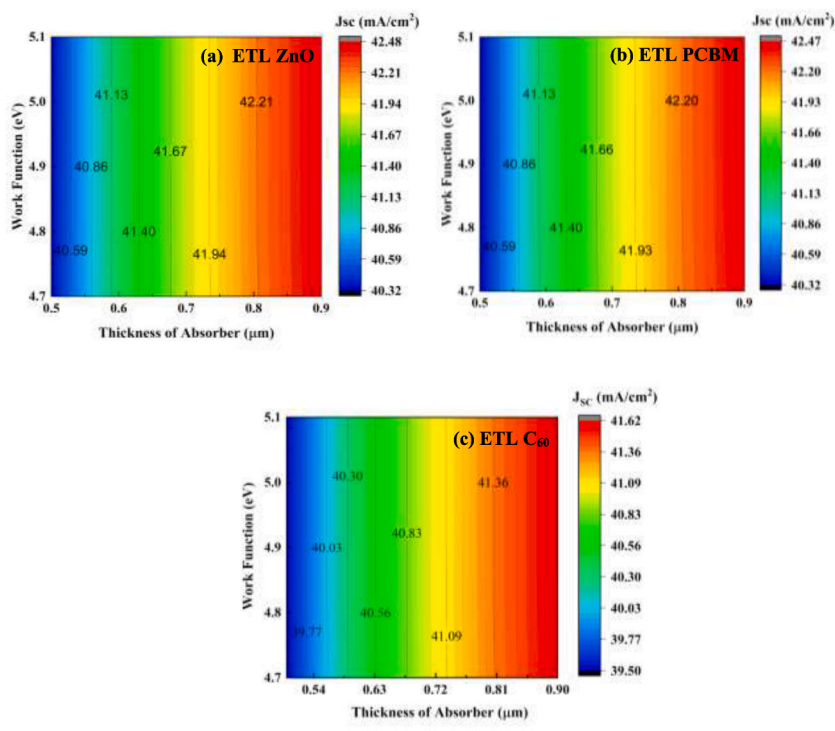
Fig. 7. Contour plots illustrating the variation in J_{SC} for AgCdF$_3$-based SC when (a) ZnO, (b) PCBM, and (c) C$_{60}$ ETLs were incorporated, in addition to the concurrent changes in absorber layer thickness and work function.
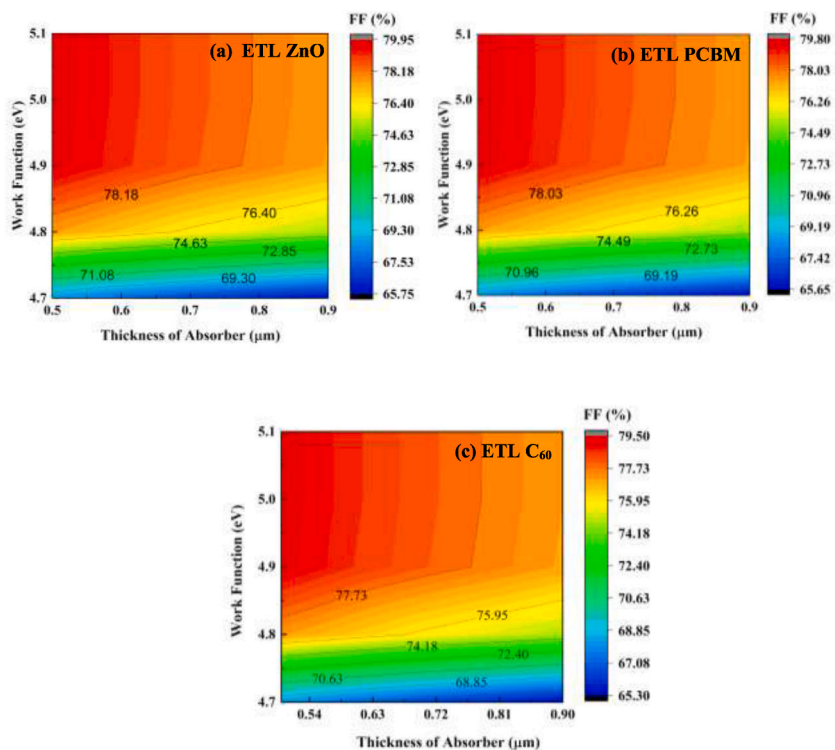
Fig. 8. Contour plots illustrating the variation in FF for AgCdF$_3$-based SC when (a) ZnO, (b) PCBM, and (c) C$_{60}$ ETLs were incorporated, in addition to the concurrent changes in absorber layer thickness and work function.

and metal work function. The effect of increasing absorber thickness in the value of FF shows a decreasing trend due to the fact that in thicker absorber the internal power depletion increases which causes a reduction in FF.

Comparing the PCE among the three ETLs for the influence of absorber thickness and back contact metal work function shows the difference in values. Fig. 9a shows that the maximum PCE achieved for ZnO is 27.58 %, which is the highest among the 3 ETLs. This maximum PCE is achieved for absorber thickness in the range (0.5–0.8) micrometer and metal work function (4.9–5.1) eV. Fig. 9(b and c) shows corresponding contour plots for ETL PCBM and C_{60}, respectively, where ETL PCBM shows a maximum PCE of 27.52 % and ETL C_{60} shows a maximum of 26.80 %. For both the ETL (PCBM, C_{60}), the maximum PCE has been achieved for absorber thickness in the range (0.5–0.8) micrometer and metal work function (4.9–5.1) eV, which is the same for ETL ZnO. The PCE of PSCs is controlled by two factors, namely photon absorption and carrier transport. Photon absorption governs the power conversion efficiency (PCE) in thinner absorbers, while carrier transport governs the PCE in thicker absorbers. So, there exists an optimum value of absorber thickness (0.5–0.8) micrometer for $AgCdF_3$ which corresponds to higher PCE. Above the optimum thickness of the absorber, there exists higher number of excess carriers and more traps which pose the opportunity for the carrier recombination leading to lower PCE. The increase of metal work function leads to higher PCE due to the fact that the barrier height of majority carrier decreases with the increase in metal work function which makes contact more ohmic.

### 3.2.4. Effect of absorber and ETL thickness on PV performance

In order to achieve optimal performance in the production of supercapacitors, it is essential to carefully choose and combine the appropriate ETL and absorber materials. The appropriate thickness of the absorber and ETL may play a significant role in enhancing light harvesting and facilitating efficient carrier transit. The placement of the ETL, situated between the ITO and absorber layer, has a notable impact on the photon coupling inside the absorber layer.

The study of thickness for the ETL has significance due to its potential to cause parasitic absorption inside the ETL, thereby diminishing photon coupling in the absorber layer. In this study, we assessed the impact of the $AgCdF_3$ absorber's thickness as well as the thickness of the ZnO, PCBM, and C_{60} ETLs on the performance of PSCs. Fig. 10(a and b) illustrate the comparable behavior of ETL ZnO and PCBM, with both obtaining a maximum V_{OC} of 0.8533 V & 0.8531 V, respectively. These values were obtained when the thickness of the absorber layer was below 0.53 μm, and the thickness of the ETL was below 0.09 μm. However, Fig. 10c demonstrates a distinct pattern for the C_{60} ETL, where greater concentrations of V_{OC} may be attained with an absorber thickness below 0.52 μm and an ETL thickness ranging from 0.063 μm. The ZnO ETL-based structure exhibited the highest observed value of volatile organic compounds (V_{OC}). Hence, there exists an inverse relationship between the V_{OC} & the thicknesses of the absorber and ETL.

Fig. 11(a and b) demonstrate a similar trend for ZnO and PCBM ETL-based solar cells. The greatest J_{SC} values for both materials are virtually equal, measuring 42.48 and 42.44 mA/cm² respectively. These results were obtained when the absorber thickness was 0.2 μm and the ETL thickness was 0.01 μm. The C_{60}-based ETL structure exhibits the highest value of 41.62 mA/cm² for the J_{SC} as shown in Fig. 11c. This optimal performance is achieved when the absorber thickness ranges from 0.81 to 0.9 μm while the ETL thickness ranges
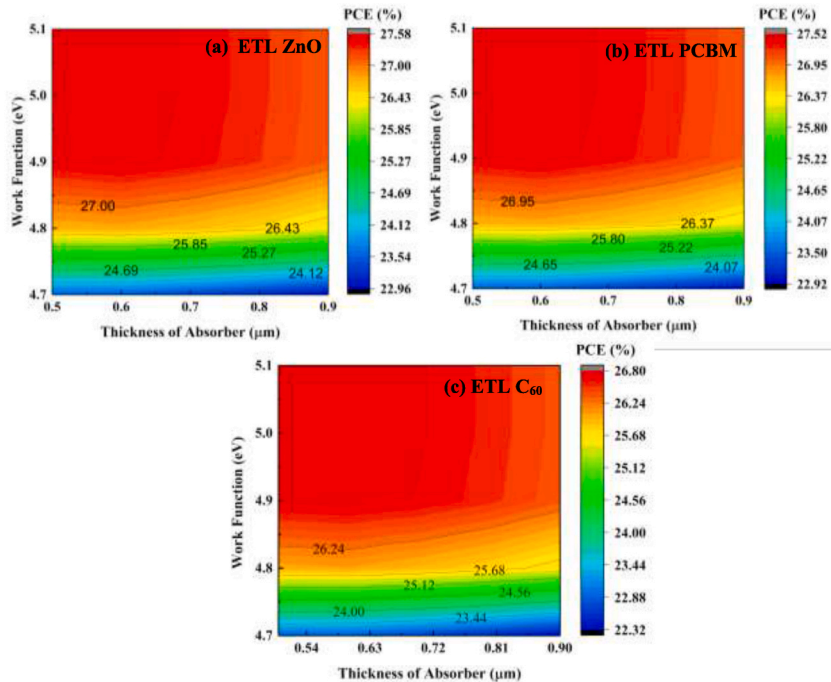
Fig. 9. Contour plots illustrating the variation in PCE for $AgCdF_3$-based SC when (a) ZnO, (b) PCBM, and (c) C_{60} ETLs were incorporated, in addition to the concurrent changes in absorber layer thickness and work function.
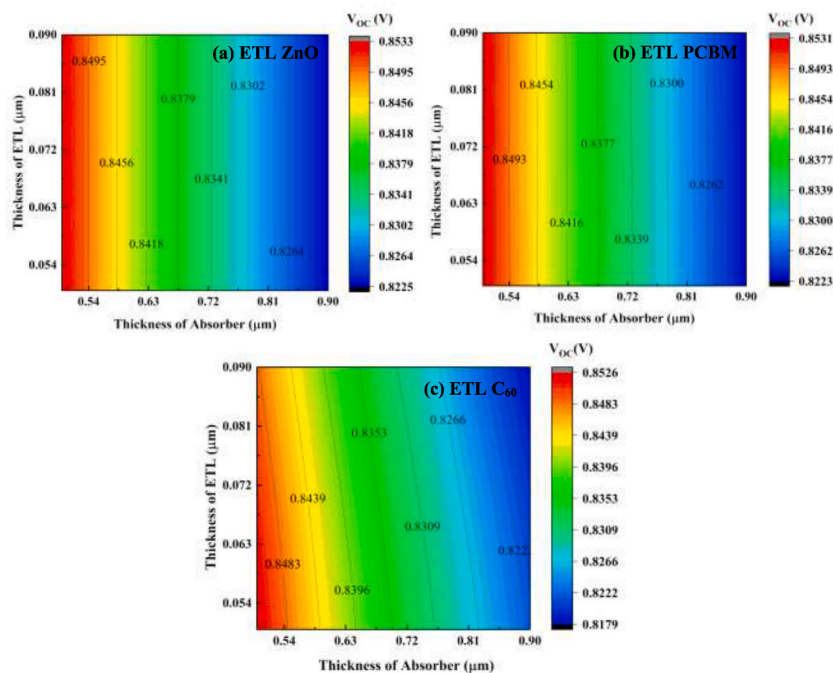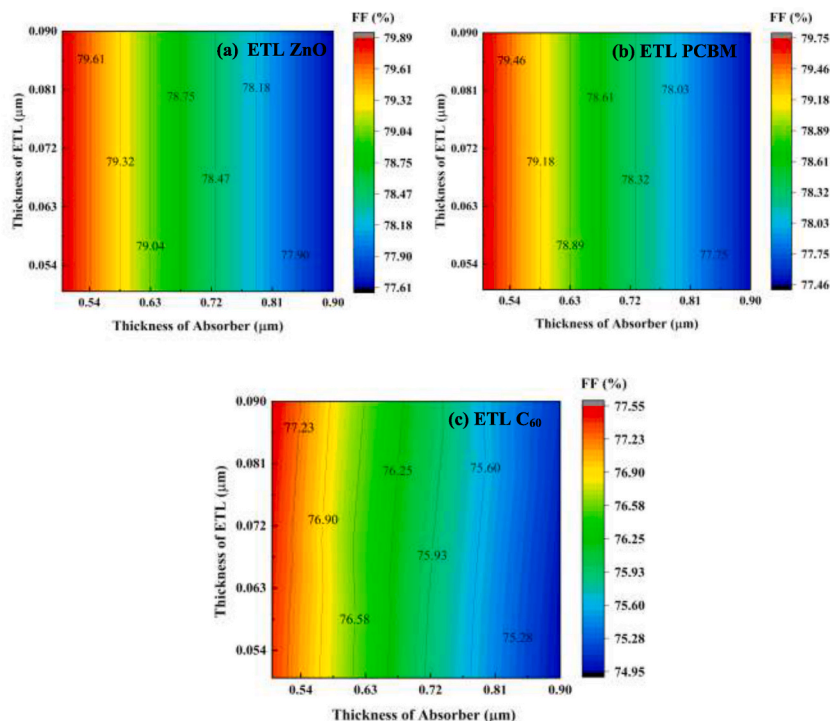
Fig. 10. Contour plots illustrating the variation in V_{OC} for AgCdF$_3$-based SC when (a) ZnO, (b) PCBM, and (c) C$_{60}$ ETLs were incorporated, in addition to the concurrent changes in ETL and absorber layer thicknesses.
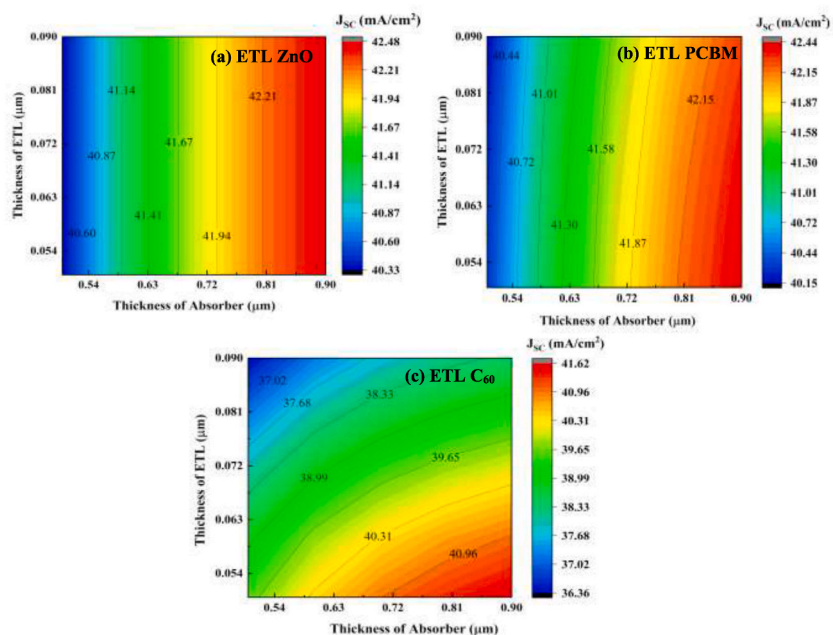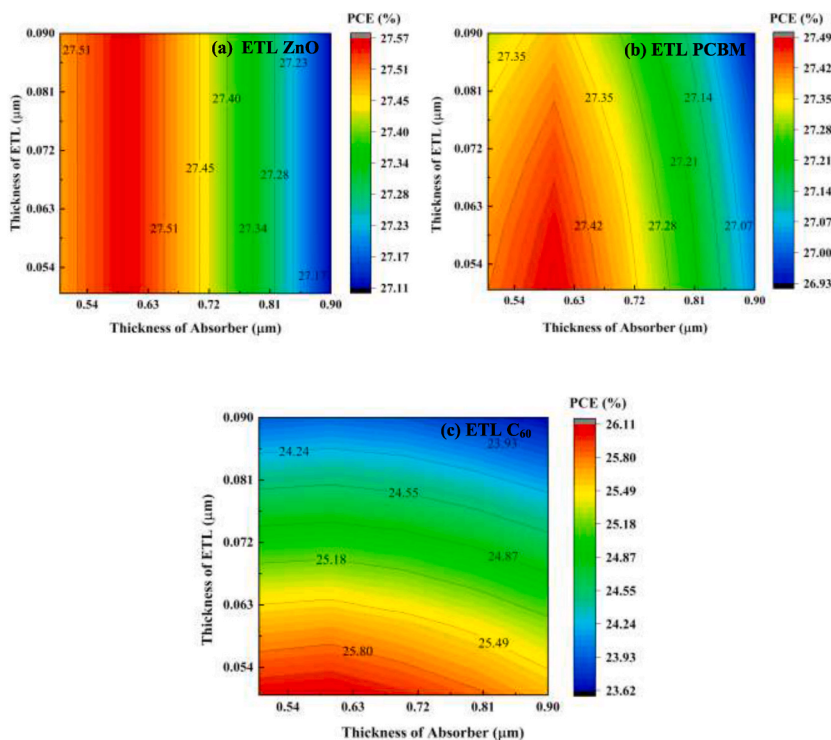

Fig. 11. Contour plots illustrating the variation in J_{SC} for AgCdF$_3$-based SC when (a) ZnO, (b) PCBM, and (c) C$_{60}$ ETLs were incorporated, in addition to the concurrent changes in ETL and absorber layer thicknesses.

from 0.05 to 0.054 μm. Fig. 12(a and b) demonstrate that ZnO and PCBM-based ETLs exhibit greater values of FF when the thickness of the absorber layer falls within the range of 0.5–0.54 μm. The independence of the FF from the thickness of the ETL is seen across all three ETLs. ZnO has the greatest FF among the materials under consideration, reaching a value of 79.89 %. This represents a marginal increase of 0.14 % compared to the FF of PCBM. C$_{60}$ exhibits a similar trend of fluctuation in FF as seen in ZnO and PCBM. However, the highest FF value attained with C$_{60}$ as the ETL is around 2.34 % and 2.2 % lower compared to ZnO and PCBM correspondingly (refer to

Fig. 12. Contour plots illustrating the variation in FF for AgCdF$_3$-based SC when (a) ZnO, (b) PCBM, and (c) C$_{60}$ ETLs were incorporated, in addition to the concurrent changes in ETL and absorber layer thicknesses.

Fig. 13. Contour plots illustrating the variation in PCE for AgCdF$_3$-based SC when (a) ZnO, (b) PCBM, and (c) C$_{60}$ ETLs were incorporated, in addition to the concurrent changes in ETL and absorber layer thicknesses.

Fig. 12c). Based on the findings, it can be inferred that the thickness of the ETL does not influence the FF value for the ETLs and reaches its peak when the absorber thickness ranges from 0.5 to 0.52 μm. The PSCs that were integrated with ZnO structures as shown in Fig. 13a and had an absorber layer thickness ranging from 0.55 to 0.66 exhibited a maximum PCE of 27.57 %. Furthermore, the PCE was found to be essentially unaffected by the thickness of the ETL. The structures based on PCBM and C_{60} exhibited comparable performance, with PCEs of around 27.49 % and 26.11 %, respectively. The absorber thicknesses ranged from 0.55 to 0.63 μm and 0.5–0.7 μm, while the ETL thicknesses ranged from 0.05 to 0.06 μm and 0.05–0.054 μm, respectively (refer to Fig. 13(b and c)). Among the various structures examined, it was observed that ZnO exhibited the PCE, whilst C_{60} had the lowest PCE. In conclusion, the present study aligns with the findings of prior research on PV.

3.2.5. Effect of series resistance

This part examines the impact of series resistances (R_S) on the performance of $AgCdF_3$ absorber-based solar cells. The value of R_S was systematically adjusted within the range of 0–6 Ω-cm^2, while the shunt resistance remained constant at 10^5 Ω-cm^2. Fig. 14(a and b) demonstrate that the values of V_{OC} and J_{SC} exhibit little dependence on the R_S for various ETLs. ZnO shows the greatest value of V_{OC}, whereas fullerene (C_{60}) displays the lowest value.

ZnO exhibits the highest recorded value of J_{SC}, whereas C_{60} has the lowest recorded value. Based on the data shown in Fig. 14(c and d), it can be seen that there exists an inverse relationship between efficiency and R_S. The sources of R_S include electrode resistance, interface contact resistance, and semiconductor resistance. The FF exhibits a decrease of 32 % from an initial value of 77.61 to a final value of 52.75, corresponding to a change in resistivity from 0 to 6 Ω-cm^2 for all ETLs. In the same manner, the PCE experiences a decrease from 27.11 % to 18.42 % for the combination of ZnO and PCBM, whereas, for C_{60}, the PCE decreases from 27.04 % to 18.36 %. This decline occurs within the range of Rs values spanning from 0 to 6 Ω-cm^2. Compared to other structures, the ITO/ZnO/$AgCdF_3$/CuI/Au PSC structure exhibited superior performance in V_{OC}, J_{SC}, FF, and PCE. Similarly, the ITO/C_{60}/$AgCdF_3$/CuI/Au PSC structure also showed the lowest levels of V_{OC}, J_{SC}, FF, and PCE performance.

3.2.6. Effect of shunt resistance

Various components contribute to internal resistances, including charge-collecting interlayers, metal-based electrodes, light-absorbing materials, and interface barriers [67]. The anticipated response of a solar cell's current-voltage (J-V) characteristic, when subjected to optimal one-sun illumination circumstances, may be elucidated via the use of the Shockley equation (Eqs. (20) and (21)) [68].

$$J_{SC} = J_{PH} - J_O \left[exp\left(\frac{q_e(V - JR_s)}{nkT_e}\right) - 1 \right] - \frac{V - JR_s}{R_{Sh}} \tag{20}$$

$$V_{OC} = \left(\frac{nkT_e}{q_e}\right) ln \left\{ \frac{J_{PH}}{J_o} \left(1 - \frac{V_{OC}}{J_{PH}R_{Sh}}\right) \right\} \tag{21}$$

In this context, the symbol "q_e" represents the elementary charge, "J_{PH}" denotes the photocurrent density, "J_o" represents the reverse bias saturation current density, "R_S" signifies the series resistance, "R_{Sh}" represents the shunt resistance, "n" denotes the diode ideality factor, "k" symbolizes the Boltzmann constant (1.38×10^{23} J K^{-1}), and "T_e" represents the ambient temperature (298 K).

The graphical representations in Fig. 15(a–d) illustrates the impact of R_{Sh} on key parameters such as V_{OC}, J_{SC}, FF, and PCE. The range of R_{Sh} values explored in the study spans from 10 to 10^7 Ω-cm^2, whereas a fixed R_S value of 0.5 Ω cm^2 was maintained throughout all photovoltaic structures. The three ETL structures exhibited a consistent pattern of growing R_{Sh}, whereas the PV parameters saw a fast rise from 10 to 10^2 Ω-cm^2. The dependence of the PV parameters, namely V_{OC}, FF, and PCE, on the R_{Sh} is evident for three ETLs. However, the J_{SC} of ZnO and PCBM exhibits minimal sensitivity to variations in R_{Sh}, as depicted in Fig. 15b. Conversely, for C_{60}, J_{SC} initially increases with R_{Sh} values ranging from 10 to 10^2 Ω cm^2, but beyond 10^3 Ω cm^2, it becomes independent as well. The J_{SC} (short-circuit current density) values for ZnO and PCBM are reported as 42.45 mA/cm^2. In the case of C_{60}, the J_{SC} value shows a rise from 39.63 to 41.61 mA/cm^2. As the R_{Sh} grows from 10 to 10^2 Ω cm^2, the open-circuit voltage (V_{OC}) exhibits a significant jump from 0.42 to 0.82 V. Additionally, the FF increases from 25.03 to 65.15 %, and the PCE climbs from 4.49 to 22.4 %. Following this increase, once the R_{Sh} value exceeded 10^3 Ω cm^2, the PV parameters exhibited no further dependence on R_{Sh}. The primary factor contributing to the emergence of R_{Sh} may be attributed to manufacturing defects. Once the R_{Sh} threshold is surpassed, the p-n junction facilitates a pathway of reduced resistance for the passage of the junction current. Hence, in order to achieve the highest PCE in a heterostructure of ITO/ETL/$AgCdF_3$/CuI/Au PSCs, it is necessary to maintain a R_{Sh} value of 10^3 Ω cm^2.

3.2.7. Effect of capacitance and Mott-Schottky

Fig. 16(a–c) depict the impact of capacitance and Mott-Schottky (MS) values on three different configurations of silver cadmium fluoride ($AgCdF_3$)-based PSCs. The applied voltage ranged from 0 to 1.2 V, while the frequency remained constant at 1 MHz. Fig. 16 (a–c) illustrate the relationship between the supply voltage & capacitance, indicating an exponential rise in capacitance until it reaches a state of saturation. Fig. 16a and b displays the electrical behavior of ZnO and PCBM as ETL components in PSC structures. The capacitance of these structures exhibited an exponential growth pattern above 0.8 V. Conversely, in Fig. 16c, C_{60} as an ETL material had a similar growing trend in capacitance, although this behavior was seen at a somewhat lower voltage threshold of 0.6 V. The structure with a ZnO ETL had the maximum capacitance, measuring 13745.1228 C (nF/cm^2), while the ETL composed of C_{60} demonstrated the lowest capacitance. The approach used for the investigation of space charge distributions in semiconductors is MS
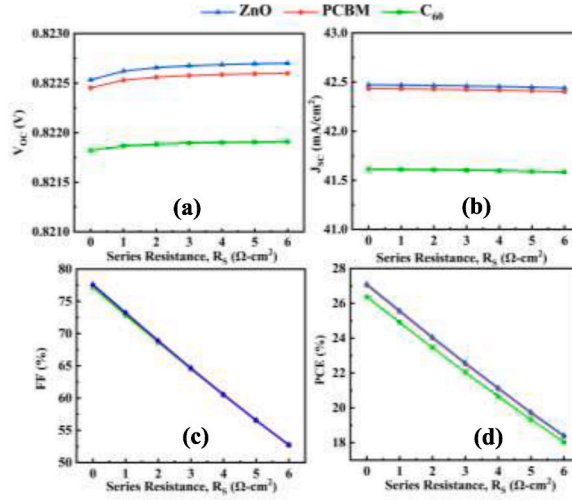
Fig. 14. The impact of R_S variation on PV parameters (a) V_{OC}, (b) J_{SC}, (c) FF, and (d) PCE for various ETLs with a constant R_{Sh}.
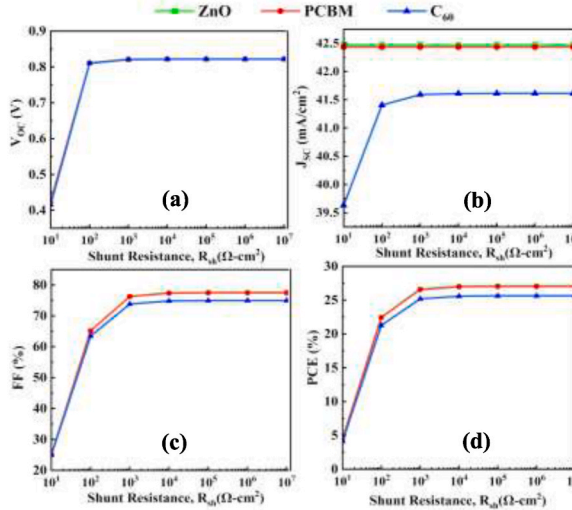
Fig. 15. The impact of R_{Sh} variation on PV parameters (a) V_{OC}, (b) J_{SC}, (c) FF, and (d) PCE for various ETLs with a constant R_S.

analysis, as seen in Fig. 16. The device exhibits a depletion state under no bias conditions; however, the depletion breadth decreases when a forward bias of about 0.5 V is introduced. The relationship between the forward bias voltage and the capacitance is directly proportional.

Fig. 16(a–c) illustrate that the three ETLs exhibit comparable MS values. The structure of ZnO and PCBM had a lower MS value of 0.1232 $1/C^2$ and 0.12379 $1/C^2$, respectively, in comparison to C_{60}, which demonstrated the highest MS value of 0.12384 $1/C^2$.

3.2.8. Effect of generation and recombination rate

Fig. 17(a and b) illustrate the rates of carrier production and recombination in three PSCs based on $AgCdF_3$, as observed throughout a depth range of 0–1.5 μm. The process by which an electron transitions to the conduction band is facilitated by the absorption of energy, resulting in the creation of a vacancy in the valence band known as a hole. This event leads to the formation of an electron-hole pair. The generation of carriers is initiated by the emission of electrons and holes. The largest generation rates occur within the range of 1.0–1.05 μm, with the ITO/ZnO/AgCdF₃/CuI/Au configuration exhibiting the highest generation rate. The devices exhibited maxima in generation at wavelengths of 1 and 1.05 μm. However, at a wavelength of 1 μm, the observed generation rate was found to be greater compared to the generation rate at 1.05 μm. ZnO has the greatest generation rate, quantified at 2×10^{22} cm^3s^{-1}. Similarly, other Extract, Transform, and Load (ETL) processes also exhibit a comparable pace of creation. In order to determine the number of electron-hole pairs that contribute to the function G(x), SCAPS-1D utilizes the incoming photon flux, denoted as Nphot (λ, x) [69].

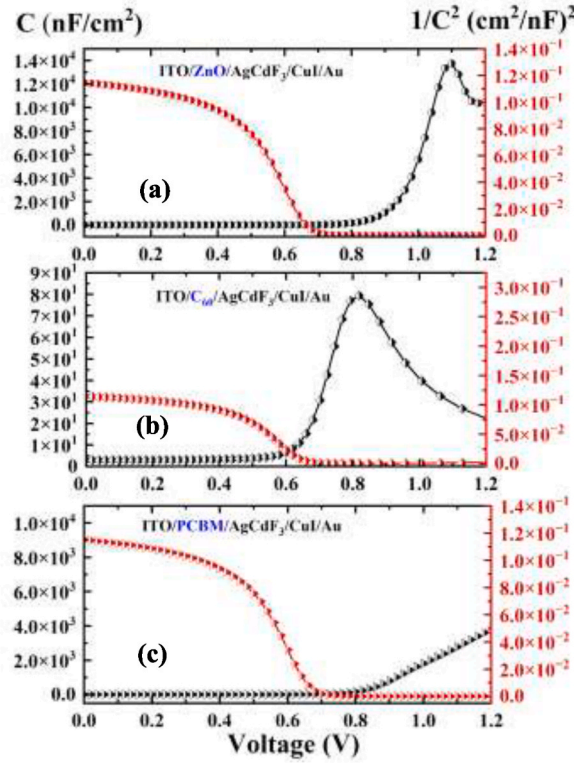**Fig. 16.** Capacitance and Mott−Schottky $(1/C^2)$ plot for the AgCdF$_3$ perovskite solar cell with distinct ETLs: (a) ZnO, (b) C$_{60}$, and (c) PCBM.
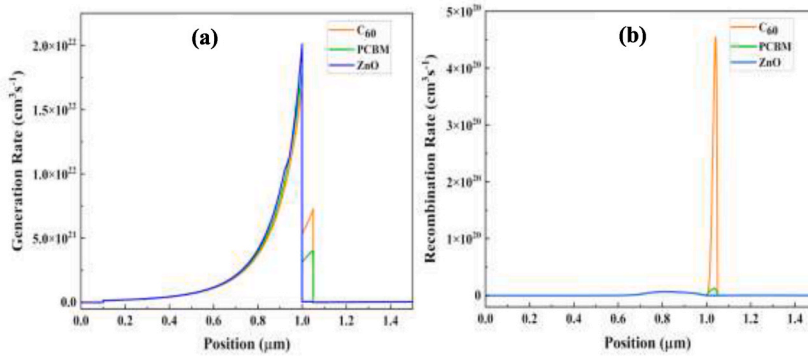

Fig. 17. (a) Generation rate and (b) recombination rate for AgCdF$_3$-based perovskite solar cell structures with three different ETLs.

$$\mathbf{G}(\lambda, \mathbf{x}) = \mathbf{a}(\lambda, \mathbf{x}) \times \mathbf{N}_{\text{phot}}(\lambda, \mathbf{x}) \tag{22}$$

The phenomenon of recombination involves the many mechanisms by which electron-hole pairs recombine, leading to the combining and subsequent separation of electrons and holes within the conduction band. The recombination rate inside a solar cell is influenced by the lifetime and concentration of the charge carrier. The occurrence of defect states inside the absorber layer, as well as at the interfaces, results in an augmentation of the recombination process of electron-hole pairs. The recombination profile of electron-hole pairs inside the solar cell is subject to the impact of energy state production. The uneven distribution of recombination rates may be ascribed to the existence of defects and grain boundaries [69]. The devices that were analyzed demonstrated their maximum recombination rates within the region of 1.0–1.05 μm. Nevertheless, the configuration of ITO/C$_{60}$/AgCdF$_3$/CuI/Au ETL exhibited the most notable recombination peak, as seen. The primary cause of recombination losses may be ascribed to the energy levels that arise inside the intermediate area between the valence and conduction bands. The existence of grain boundaries and intrinsic inadequacies that occur during the construction of junctions and structures may be responsible for the uneven distribution of recombination rates in PSCs. C$_{60}$ shows a notable increase in recombination peaks with a rate of 4.5×10^{20} cm^{3}s^{-1}. In contrast, ZnO and PCBM display insignificant recombination rates at most sites, except for the region of 0.7–1.05 μm, where a minor value is seen. However, this value

remains substantially lower than that of C_{60}.

3.2.9. Effect of temperature

Charge extraction is adversely affected by temperature-induced performance losses resulting from incoming solar radiation, which have a detrimental effect on the overall performance of the system [70]. Previous research has shown that the mechanical integrity of perovskite solar cells is influenced by the disparity between the thermal expansion coefficients and the low fracture energy of the layers [71]. The process of solar concentration enhances the temperature elevation inside the PSC by augmenting the influx of photons. Concentrator photovoltaic systems use the enhanced light concentration to amplify the photogenerated current, therefore facilitating the conversion of incoming radiation into electrical power [72]. The reduction in V_{OC} and consequent decrease in power output of the solar cell system is attributed to the dark current, which is influenced by the operating temperature. The temperature sensitivity of the open-circuit voltage is of utmost importance, as it accounts for 80–90 % of the temperature coefficient of efficiency. PSCs have garnered significant interest within the PV field. However, despite their potential, PSCs tend to demonstrate thermal instability when subjected to frequent light exposure. For example, the performance of PSCs experiences a degradation of 10 % during a very short duration of 1000 h when operated at a temperature of 85 °C [73,74]. This degradation occurs at a substantially faster rate compared to the lifespan of silicon SCs. Furthermore, the use of temperature as a therapeutic intervention for individual layers or the whole of PSCs may be employed as the ambient temperature during simulation experiments. Therefore, in order to ensure the viability of PSCs for future commercial applications, it is essential to comprehensively investigate the impact of temperature on their performance, taking into account the variability of temperature values. Fig. 18 depicts the impact of temperature variations ranging from 300 to 450 K on the performance metrics, namely V_{OC}, J_{SC}, FF, and PCE, for the three devices. These measurements were taken while subjecting the devices to an illumination intensity of 100 mW/cm^2 of solar radiation.

Based on the data shown in Fig. 18a, it can be seen that the V_{OC} exhibited a declining trend across all solar cell configurations, each including a distinct ETL. This decline may be attributed to the rise in temperature, which leads to an increase in the reverse saturation current. The curves representing the three ETLs exhibit a high degree of similarity. Equations (23) and (24) establish the relationship between V_{OC} and temperature [75,76].

$$V_{OC} = \frac{nKT}{q} \log\left(\frac{J_{SC}}{J_o} + 1\right) \tag{23}$$

$$\frac{d(V_{OC})}{dT} = \frac{V_{OC}}{T} - \frac{\frac{E_g}{q}}{T} \tag{24}$$

Here, J_O, E_g, T, q, n, and k are the respective symbols for reverse saturation current, band gap, temperature, electronic charge, ideality factor, and Boltzmann constant.
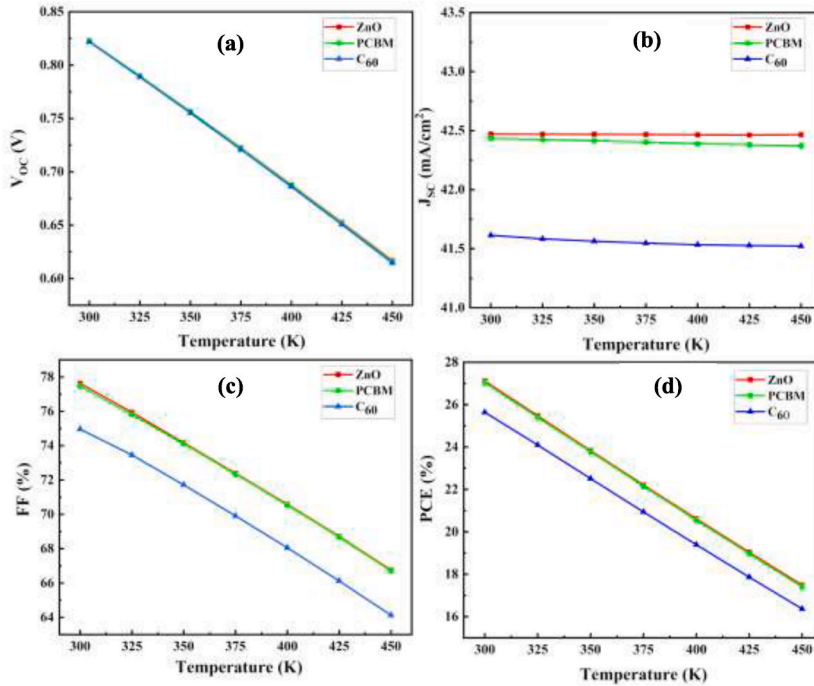

Fig. 18. The impact of temperature variation on the PV parameters (a) V_{OC}, (b) J_{SC}, (c) FF, and (d) PCE for various ETLs.

J_{SC} of the three ETLs exhibits a consistent trend, with a marginal decline seen as the temperature rises. This behavior is visually shown in Fig. 18b. ZnO has the greatest value of J_{SC} at 42.5 mA/cm2, whilst C_{60} shows the lowest value at 41.8 mA/cm^2. The J_{SC} values reached their maximum at a temperature of 300 K, mostly due to the thermal production of carriers in conjunction with an appropriate band gap.

Moreover, when examining Fig. 18c at higher temperatures, it can be observed that FF exhibits a declining trend in the instances of ITO/ZnO/AgCdF$_3$/CuI/Au, ITO/C$_{60}$/AgCdF$_3$/CuI/Au, and ITO/PCBM/AgCdF$_3$/CuI/Au. This can be attributed to the influence of temperature on the effective band gap of the material, as well as the carrier density and mobility within the device. Based on the data shown in Fig. 18c, it can be seen that the solar cell configuration, including ZnO and PCBM as the ETL, exhibited a comparatively greater FF of around 75 %. In contrast, the FF values for solar cells incorporating C$_{60}$ structures were found to be lower than 75 %, with a decreasing trend observed as the temperature increased.

Furthermore, the PCE pattern exhibits a declining trend in relation to temperature for three distinct solar cell configurations. Based on the data shown in Fig. 18d, it can be seen that the initial performance of the PCBM and ZnO as ETL exhibited an approximate PCE of 27 %, but the C$_{60}$ ETL demonstrated a PCE of around 26 %, indicating a small decrease in efficiency.

Fig. 18 illustrates the varying trends of solar cell characteristics with various transport layers in response to temperature changes. Certain variables exhibit a decrease in response as temperature rises, whereas others maintain a consistent level of response. The PV characteristics exhibit a decrease when temperature rises, perhaps attributable to an elevation in recombination phenomena that subsequently diminishes the efficiency of the solar cell. An increase in temperature generally results in a rise in the carrier recombination rate, hence causing a decline in the solar cell efficiency. The lack of temperature dependence seen in some parameters may be attributed to a delicate equilibrium between the opposing influences of enhanced carrier production and augmented recombination. In these instances, the potential rise in carrier production coming from elevated temperatures is counteracted by a similar increase in recombination, leading to an equilibrium state where the solar cell characteristics remain unchanged.

4. Conclusion

Several appealing characteristics, including the optimal indirect band gap, high absorption coefficient, low exciton binding energy, and enhanced carrier mobility, have made AgCdF$_3$ the preferred absorber material for lead-free PV applications. The band gap of AgCdF$_3$ was estimated 1.106eV along with a notable absorption coefficient, reduced reflectivity, and enhanced conductivity. Mechanical properties reveal AgCdF$_3$ is mechanically stable, ductile in nature, and machinable. It is evident that PSCs using ETL like ZnO and PCBM resulted in greater efficiencies (>27 %) for the ITO/ETL/AgCdF$_3$/CuI/Au heterostructures, however another ETL, C$_{60}$, showed lower efficiency (<27 %). The band alignment of the perovskite AgCdF$_3$, HTL, and ETL has a major influence on PV performance. The study of several SC structures shows that ITO/ZnO/AgCdF$_3$/CuI/Au performs the best, as evidenced by its PCE of 27.12 %, FF of 77.62 %, J_{SC} of 42.47 mA/cm^2, and V_{OC} of 0.823 V. A comprehensive investigation shows work function of 5eV or higher, lower series and higher shunt resistance, along with an operating temperature of 300 K can show the best PCE for the analyzed configurations. A thorough knowledge of the mechanisms driving PV performance is achieved by analyzing the Mott-Schottky, capacitance, generation, and recombination rates associated with these devices. For the purpose of creating high-performance and inexpensive AgCdF$_3$ perovskite solar cells, this meticulous investigation may pave the way for successful outcomes.

Data availability

Data can be made available on request.

CRediT authorship contribution statement

Fatema-Tuz- Zahra: Writing – original draft, Formal analysis, Data curation, Conceptualization. **Md Mehidi Hasan:** Writing – original draft, Software, Investigation, Formal analysis, Data curation. **Md. Bokhtiar Hossen:** Writing – original draft, Investigation, Formal analysis, Data curation. **Md. Rasidul Islam:** Writing – review & editing, Validation, Supervision, Investigation, Formal analysis.

Declaration of competing interest

The authors declare that they have no known competing financial interests or personal relationships that could have appeared to influence the work reported in this paper.

References

[1] T. Ye, K. Wang, Y. Hou, D. Yang, N. Smith, B. Magill, J. Yoon, R.R.H.H. Mudiyanselage, G.A. Khodaparast, K. Wang, S. Priya, Ambient-air-stable lead-free CsSnI3Solar cells with greater than 7.5% efficiency, J. Am. Chem. Soc. 143 (2021) 4319–4328, https://doi.org/10.1021/jacs.0c13069.

[2] S.D. Stranks, H.J. Snaith, Metal-halide perovskites for photovoltaic and light-emitting devices, Nat. Nanotechnol. 10 (2015) 391–402, https://doi.org/10.1038/nnano.2015.90.

[3] Y. Zhou, K. Zhu, Perovskite solar cells shine in the "valley of the sun,", ACS Energy Lett. 1 (2016) 64–67, https://doi.org/10.1021/acsenergylett.6b00069.

[4] M. Yang, Y. Zhou, Y. Zeng, C.S. Jiang, N.P. Padture, K. Zhu, Square-centimeter solution-processed planar CH3NH3PbI3 perovskite solar cells with efficiency exceeding 15, Adv. Mater. 27 (2015) 6363–6370, https://doi.org/10.1002/adma.201502586.

[5] Y. Zhou, M. Yang, S. Pang, K. Zhu, N.P. Padture, Exceptional Morphology-preserving evolution of formamidinium lead triiodide perovskite thin films via organic-cation displacement, J. Am. Chem. Soc. 138 (2016) 5535–5538, https://doi.org/10.1021/jacs.6b02787.

[6] N.S.M.N. Izam, Z. Itam, W.L. Sing, A. Syamsir, Sustainable development perspectives of solar energy technologies with focus on solar photovoltaic—a review, Energies 15 (2022) 1–15, https://doi.org/10.3390/en15082790.

[7] A. Kojima, K. Teshima, Y. Shirai, T. Miyasaka, Organometal halide perovskites as visible-light sensitizers for photovoltaic cells, J. Am. Chem. Soc. 131 (2009) 6050–6051, https://doi.org/10.1021/ja809598r.

[8] H.S. Jung, N.G. Park, Perovskite solar cells: from materials to devices, Small 11 (2015) 10–25, https://doi.org/10.1002/smll.201402767.

[9] M.A. Green, A. Ho-Baillie, H.J. Snaith, The emergence of perovskite solar cells, Nat. Photonics 8 (2014) 506–514, https://doi.org/10.1038/nphoton.2014.134.

[10] A. Thakur, D. Singh, S. Kaur Gill, Numerical simulations of 26.11% efficient planar CH3NH3PbI3 perovskite n-i-p solar cell, Mater. Today Proc. 71 (2022) 195–201, https://doi.org/10.1016/J.MATPR.2022.08.423.

[11] T. Dureja, A. Garg, S. Bhalla, D. Bhutani, A. Khanna, Double lead-free perovskite solar cell for 19.9% conversion efficiency: a SCAPS-1D based simulation study, Mater. Today Proc. 71 (2022) 239–242, https://doi.org/10.1016/J.MATPR.2022.08.518.

[12] T. Miyasaka, A. Kulkarni, G.M. Kim, S. Öz, A.K. Jena, Perovskite solar cells: can we go organic-free, lead-free, and dopant-free? Adv. Energy Mater. 10 (2020) 1–20, https://doi.org/10.1002/aenm.201902500.

[13] Y. Rong, Y. Hu, A. Mei, H. Tan, M.I. Saidaminov, S. Il Seok, M.D. McGehee, E.H. Sargent, H. Han, Challenges for commercializing perovskite solar cells, Science (2018) 361, https://doi.org/10.1126/science.aat8235.

[14] E. Smecca, Y. Numata, I. Deretzis, G. Pellegrino, S. Boninelli, T. Miyasaka, A. La Magna, A. Alberti, Stability of solution-processed MAPbI3 and FAPbI3 layers, Phys. Chem. Chem. Phys. 18 (2016) 13413–13422, https://doi.org/10.1039/c6cp00721j.

[15] Shakeel, A.H. Reshak, S. Khan, A. Laref, G. Murtaza, J. Bila, Pressure induced physical variations in the lead free fluoropervoskites XYF3 (X=K, Rb, Ag; Y=Zn, Sr, Mg): optical materials, Opt. Mater. 109 (2020) 110325, https://doi.org/10.1016/j.optmat.2020.110325.

[16] M. Eibschütz, H.J. Guggenheim, Antiferromagnetic-piezoelectric crystals: BaMe4 (M = Mn, Fe, Co and Ni), Solid State Commun. 6 (1968) 737–739, https://doi.org/10.1016/0038-1098(68)90576-0.

[17] M. Sahnoun, M. Zbiri, C. Daul, R. Khenata, H. Baltache, M. Driz, Full potential calculation of structural, electronic and optical properties of KMgF3, Mater. Chem. Phys. 91 (2005) 185–191, https://doi.org/10.1016/J.MATCHEMPHYS.2004.11.019.

[18] G. Hörsch, H.J. Paus, A new color center laser on the basis of lead-doped KMgF3, Opt Commun. 60 (1986) 69–73, https://doi.org/10.1016/0030-4018(86)90119-7.

[19] R. Hua, B. Lei, D. Xie, C. Shi, Synthesis of the complex fluoride LiBaF3 and optical spectroscopy properties of LiBaF3:M(M=Eu,Ce) through a solvothermal process, J. Solid State Chem. 175 (2003) 284–288, https://doi.org/10.1016/S0022-4596(03)00282-2.

[20] A.V. Gektin, I.M. Krasovitskaya, N.V. Shiran, High-temperature thermoluminescence of KMgF3-based crystals, J. Lumin. 72–74 (1997) 664–666, https://doi.org/10.1016/S0022-2313(96)00231-1.

[21] F. Zhang, Y. Mao, T.J. Park, S.S. Wong, Green synthesis and property characterization of single-crystalline perovskite fluoride nanorods, Adv. Funct. Mater. 18 (2008) 103–112, https://doi.org/10.1002/adfm.200700655.

[22] W. Pu, W. Xiao, J. Wang, X. Li, L. Wang, Screening of perovskite materials for solar cell applications by first-principles calculations, Mater. Des. 198 (2021) 109387, https://doi.org/10.1016/j.matdes.2020.109387.

[23] F.T. Zahra, M.M. Islam, M.M. Hasan, M.R. Islam, S. Ahmad, DFT insights into the pressure-induced ultraviolet to visible band gap engineering of TlMgF3 cubic halide perovskites for optoelectronic applications, J. Phys. Chem. Solids 191 (2024) 112037, https://doi.org/10.1016/J.JPCS.2024.112037.

[24] M.T. Hossain, M.M. Hasan, F.-T. Zahra, S. Swargo, R. Al-Arefeen Dhroobo, M.R. Al Amin, F.M.A. Sieam, S.T. Disha, M.R. Islam, A comprehensive DFT investigation of inorganic halide perovskites GaXCl3 (X = Ca, Sr, and Ba) for optoelectronics application, Phys. B Condens. Matter (2024) 416131, https://doi.org/10.1016/J.PHYSB.2024.416131.

[25] M.I. Hussain, R.M.A. Khalil, F. Hussain, A.M. Rana, M. Imran, Ab-initio prediction of the mechanical, magnetic and thermoelectric behaviour of perovskite oxides XGaO3 (X = Sc, Ti, Ag) using LDA+U functional: for optoelectronic devices, J. Mol. Graph. Model. 99 (2020) 107621, https://doi.org/10.1016/j.jmgm.2020.107621.

[26] U.A. Khan, N.U. KhanAbdullah, A.H. Alghtani, V. Tirth, S.J. Ahmed, M. Sajjad, A. Algahtani, T. Shaheed, A. Zaman, First-principles investigation on the structural, electronic, mechanical and optical properties of silver based perovskite AgXCl3(X= Ca, Sr), J. Mater. Res. Technol. 20 (2022) 3296–3305, https://doi.org/10.1016/j.jmrt.2022.08.101.

[27] A. Mahmood, S.M. Ramay, H.M. Rafique, Y. Al-Zaghayer, S.U.D. Khan, First-principles study of electronic, optical and thermoelectric properties in cubic perovskite materials AgMO3 (M = V, Nb, Ta), Mod. Phys. Lett. B 28 (2014) 1–12, https://doi.org/10.1142/S0217984914500778.

[28] H.L. Sun, C.L. Yang, M.S. Wang, X.G. Ma, Y.G. Yi, High thermoelectric efficiency fluoride perovskite materials of AgMF3 (M = Zn, Cd), Mater. Today Energy 19 (2021) 100611, https://doi.org/10.1016/j.mtener.2020.100611.

[29] N. Shrivastav, S. Kashyap, J. Madan, A.K. Al-Mousoi, M.K.A. Mohammed, M. Khalid Hossain, R. Pandey, J. Ramanujam, Perovskite-CIGS monolithic tandem solar cells with 29.7% efficiency: a numerical study, Energy Fuels 37 (2023) 3083–3090, https://doi.org/10.1021/acs.energyfuels.2c03973.

[30] S. Kashyap, J. Madan, M.K.A. Mohammed, M. Khalid Hossain, S. Ponnusamy, R. Pandey, Unlocking the potential of MgF2 textured surface in enhancing the efficiency of perovskite solar cells, Mater. Lett. 339 (2023) 134096, https://doi.org/10.1016/J.MATLET.2023.134096.

[31] R. Pandey, S. Bhattarai, K. Sharma, J. Madan, A.K. Al-Mousoi, M.K.A. Mohammed, M. Khalid Hossain, Halide composition engineered a non-toxic perovskite–silicon tandem solar cell with 30.7% conversion efficiency, ACS Appl. Electron. Mater. 5 (2023) 5303–5315, https://doi.org/10.1021/acsaelm.2c01574.

[32] Y. Gan, X. Bi, Y. Liu, B. Qin, Q. Li, Q. Jiang, P. Mo, Numerical investigation energy conversion performance of tin-based perovskite solar cells using cell capacitance simulator, Energies 13 (2020) 5907, https://doi.org/10.3390/en13225907.

[33] Y.F. Chiang, J.Y. Jeng, M.H. Lee, S.R. Peng, P. Chen, T.F. Guo, T.C. Wen, Y.J. Hsu, C.M. Hsu, High voltage and efficient bilayer heterojunction solar cells based on an organic-inorganic hybrid perovskite absorber with a low-cost flexible substrate, Phys. Chem. Chem. Phys. 16 (2014) 6033–6040, https://doi.org/10.1039/c4cp00298a.

[34] S. Ryu, J.H. Noh, N.J. Jeon, Y. Chan Kim, W.S. Yang, J. Seo, S. Il Seok, Voltage output of efficient perovskite solar cells with high open-circuit voltage and fill factor, Energy Environ. Sci. 7 (2014) 2614–2618, https://doi.org/10.1039/c4ee00762j.

[35] A. Rashid bin Mohd Yusoff, M. Khaja Nazeeruddin, Organohalide lead perovskites for photovoltaic applications, J. Phys. Chem. Lett. 7 (2016) 851–866, https://doi.org/10.1021/acs.jpclett.5b02893.

[36] Y. Raoui, H. Ez-Zahraouy, N. Tahiri, O. El Bounagui, S. Ahmad, S. Kazim, Performance analysis of MAPbI3 based perovskite solar cells employing diverse charge selective contacts: simulation study, Sol. Energy 193 (2019) 948–955, https://doi.org/10.1016/J.SOLENER.2019.10.009.

[37] M.K. Basher, S.M. Shah Riyadh, M.K. Hossain, M. Hassan, M.A.R. Akand, S.M. Amir-Al Zumahi, M.A. Matin, N. Das, M. Nur-E-Alam, Development of zinc-oxide nanorods on chemically etched zinc plates suitable for high-efficiency photovoltaics solar cells, Opt. Quantum Electron. 55 (2023) 1–17, https://doi.org/10.1007/s11082-022-04474-1.

[38] M.K. Hossain, G.F.I. Toki, D.P. Samajdar, M. Mushtaq, M.H.K. Rubel, R. Pandey, J. Madan, M.K.A. Mohammed, M.R. Islam, M.F. Rahman, H. Bencherif, Deep insights into the coupled optoelectronic and photovoltaic analysis of lead-free CsSnI3 perovskite-based solar cell using DFT calculations and SCAPS-1D simulations, ACS Omega 8 (2023) 22466–22485, https://doi.org/10.1021/acsomega.3c00306.

[39] M.M. Khatun, A. Sunny, S.R. Al Ahmed, Numerical investigation on performance improvement of WS2 thin-film solar cell with copper iodide as hole transport layer, Sol. Energy 224 (2021) 956–965, https://doi.org/10.1016/J.SOLENER.2021.06.062.

[40] S. Tariq Jan, M. Noman, Influence of layer thickness, defect density, doping concentration, interface defects, work function, working temperature and reflecting coating on lead-free perovskite solar cell, Sol. Energy 237 (2022) 29–43, https://doi.org/10.1016/J.SOLENER.2022.03.069.

[41] X. Rong, H. Tian, W. Bi, H. Jin, T. Zhang, D. Guo, K. Zhao, Impact of metal electrode work function of CH3NH3PbI3/p-Si planar heterojunction perovskite solar cells, Sol. Energy 158 (2017) 424–431, https://doi.org/10.1016/J.SOLENER.2017.08.050.

[42] J.P. Perdew, A. Ruzsinszky, G.I. Csonka, O.A. Vydrov, G.E. Scuseria, L.A. Constantin, X. Zhou, K. Burke, Restoring the density-gradient expansion for exchange in solids and surfaces, Phys. Rev. Lett. 100 (2008) 1–4, https://doi.org/10.1103/PhysRevLett.100.136406.

[43] S.J. Clark, M.D. Segall, C.J. Pickard, P.J. Hasnip, M.I.J. Probert, K. Refson, M.C. Payne, First principles methods using CASTEP, Z. Krist 220 (2005) 567–570, https://doi.org/10.1524/zkri.220.5.567.65075.

[44] J.M. Smith, S.P. Jones, L.D. White, Rapid communication, Gastroenterology 72 (1977) 193, https://doi.org/10.1016/S0016-5085(77)80340-5.

[45] M.F. Rahman, M.M. Alam Moon, M.K. Hossain, M.H. Ali, M.D. Haque, A. Kuddus, J. Hossain, A.B. Abu, Concurrent investigation of antimony chalcogenide (Sb2Se3 and Sb2S3)-based solar cells with a potential WS2 electron transport layer, Heliyon 8 (2022) e12034, https://doi.org/10.1016/j.heliyon.2022.e12034.

[46] M.K. Hossain, M.K.A. Mohammed, R. Pandey, A.A. Arnab, M.H.K. Rubel, K.M. Hossain, M.H. Ali, M.F. Rahman, H. Bencherif, J. Madan, M.R. Islam, D. P. Samajdar, S. Bhattarai, Numerical analysis in DFT and SCAPS-1D on the influence of different charge transport layers of CsPbBr3 perovskite solar cells, Energy Fuel. 37 (2023) 6078–6098, https://doi.org/10.1021/acs.energyfuels.3c00035.

[47] H. Bencherif, M. Khalid Hossain, Design and numerical investigation of efficient (FAPbI3)1−x(CsSnI3)x perovskite solar cell with optimized performances, Sol. Energy 248 (2022) 137–148, https://doi.org/10.1016/j.solener.2022.11.012.

[48] N. Gamal, S.H. Sedky, A. Shaker, M. Fedawy, Design of lead-free perovskite solar cell using Zn1-xMgxO as ETL: SCAPS device simulation, Optik 242 (2021) 167306, https://doi.org/10.1016/j.ijleo.2021.167306.

[49] S. Bhattarai, M.K. Hossain, J. Madan, R. Pandey, D.P. Samajdar, P.K. Kalita, A.N.Z. Rashed, M.Z. Ansari, M. Amami, Performance improvement of CZTS-based hybrid solar cell with double hole transport layer using extensive simulation, J. Phys. Chem. Solids. 183 (2023) 111641, https://doi.org/10.1016/j.jpcs.2023.111641.

[50] R.A. Jabr, M. Hamad, Y.M. Mohanna, Newton-Raphson solution of Poisson's equation in a pn diode, Int. J. Electr. Eng. Educ. 44 (2007) 23–33, https://doi.org/10.7227/IJEEE.44.1.3.

[51] M.K. Hossain, M.F. Pervez, M.N.H. Mia, A.A. Mortuza, M.S. Rahaman, M.R. Karim, J.M.M. Islam, F. Ahmed, M.A. Khan, Effect of dye extracting solvents and sensitization time on photovoltaic performance of natural dye sensitized solar cells, Results Phys. 7 (2017) 1516–1523, https://doi.org/10.1016/j.rinp.2017.04.011.

[52] P. Lin, L. Lin, J. Yu, S. Cheng, P. Lu, Q. Zheng, Numerical simulation of Cu2ZnSnS4 based solar cells with In2S3 buffer layers by SCAPS-1D, J. Appl. Sci. Eng. 17 (2014) 383–390, https://doi.org/10.6180/jase.2014.17.4.05.

[53] J. Singh, H. Kaur, G. Singh, S.K. Tripathi, High thermoelectric performance in cubic inorganic halide perovskite material AgCdX3 (X = F and Cl) from first principles, Mater. Today Energy 21 (2021) 100820, https://doi.org/10.1016/j.mtener.2021.100820.

[54] N. Rahman, M. Husain, R. Khan, M. Sohail, T. Zaman, A.A. Khan, G. Murtaza, R. Neffati, A. Khan, First-principles calculations to investigate structural, elastic, optical, and thermoelectric properties of narrow band gap semiconducting cubic ternary fluoroperovskites barium based BaMF3(M = Ag and Cu) compounds, J. Mater. Res. Technol. 21 (2022) 2168–2177, https://doi.org/10.1016/j.jmrt.2022.10.037.

[55] M.M. Hossain, First-principles study on the structural, elastic, electronic and optical properties of LiNbO3, Heliyon 5 (2019) e01436, https://doi.org/10.1016/J.HELIYON.2019.E01436.

[56] F. Mouhat, F.X. Coudert, Necessary and sufficient elastic stability conditions in various crystal systems, Phys. Rev. B Condens. Matter 90 (2014) 4–7, https://doi.org/10.1103/PhysRevB.90.224104.

[57] R. Hill, Related content the elastic behaviour of a crystalline aggregate, Proc. Phys. Soc. 65 (1952) 349–354.

[58] Z. Sun, D. Music, R. Ahuja, J.M. Schneider, Theoretical investigation of the bonding and elastic properties of nanolayered ternary nitrides, Phys. Rev. B Condens. Matter 71 (2005) 3–5, https://doi.org/10.1103/PhysRevB.71.193402.

[59] M.I. Naher, S.H. Naqib, Structural, elastic, electronic, bonding, and optical properties of topological CaSn3 semimetal, J. Alloys Compd. 829 (2020) 1–26, https://doi.org/10.1016/j.jallcom.2020.154509.

[60] G. Vaitheeswaran, V. Kanchana, A. Svane, A. Delin, Elastic properties of MgCNi3 - a superconducting perovskite, J. Phys. Condens. Matter 19 (2007), https://doi.org/10.1088/0953-8984/19/32/326214.

[61] R.C. Lincoln, K.M. Koliwad, P.B. Ghate, Morse-potential evaluation of second- and third-order elastic constants of some cubic metals, Phys. Rev. 157 (1967) 463–466, https://doi.org/10.1103/PhysRev.157.463.

[62] P. Sawicka-Chudy, Z. Starowicz, G. Wisz, R. Yavorskyi, Z. Zapukhlyak, M. Bester, Ł. Głowa, M. Sibiński, M. Cholewa, Simulation of TiO 2/CuO solar cells with SCAPS-1D software, Mater. Res. Express 6 (2019) 085918, https://doi.org/10.1088/2053-1591/ab22aa.

[63] F. Jannat, S. Ahmed, M.A. Alim, Performance analysis of cesium formamidinium lead mixed halide based perovskite solar cell with MoOx as hole transport material via SCAPS-1D, Optik 228 (2021) 166202, https://doi.org/10.1016/j.ijleo.2020.166202.

[64] R. Singh, P.K. Singh, B. Bhattacharya, H.W. Rhee, Review of current progress in inorganic hole-transport materials for perovskite solar cells, Appl. Mater. Today 14 (2019) 175–200, https://doi.org/10.1016/j.apmt.2018.12.011.

[65] H. Shiel, O.S. Hutter, L.J. Phillips, J.E.N. Swallow, L.A.H. Jones, T.J. Featherstone, M.J. Smiles, P.K. Thakur, T.L. Lee, V.R. Dhanak, J.D. Major, T.D. Veal, Natural band alignments and band offsets of Sb2Se3Solar cells, ACS Appl. Energy Mater. 3 (2020) 11617–11626, https://doi.org/10.1021/acsaem.0c01477.

[66] T. Minemoto, M. Murata, Theoretical analysis on effect of band offsets in perovskite solar cells, Sol. Energy Mater. Sol. Cells 133 (2015) 8–14, https://doi.org/10.1016/j.solmat.2014.10.036.

[67] K. Tvingstedt, L. Gil-Escrig, C. Momblona, P. Rieder, D. Kiermasch, M. Sessolo, A. Baumann, H.J. Bolink, V. Dyakonov, Removing leakage and surface recombination in planar perovskite solar cells, ACS Energy Lett. 2 (2017) 424–430, https://doi.org/10.1021/acsenergylett.6b00719.

[68] Y. Li, B. Ding, Q.Q. Chu, G.J. Yang, M. Wang, C.X. Li, C.J. Li, Ultra-high open-circuit voltage of perovskite solar cells induced by nucleation thermodynamics on rough substrates, Sci. Rep. 7 (2017) 1–10, https://doi.org/10.1038/srep46141.

[69] M.K. Hossain, M.H.K. Rubel, G.F.I. Toki, I. Alam, M.F. Rahman, H. Bencherif, Effect of various electron and hole transport layers on the performance of CsPbI3-based perovskite solar cells: a numerical investigation in DFT, SCAPS-1D, and wxAMPS frameworks, ACS Omega 7 (2022) 43210–43230, https://doi.org/10.1021/acsomega.2c05912.

[70] H. Baig, H. Kanda, A.M. Asiri, M.K. Nazeeruddin, T. Mallick, Increasing efficiency of perovskite solar cells using low concentrating photovoltaic systems, Sustain. Energy Fuels 4 (2020) 528–537, https://doi.org/10.1039/c9se00550a.

[71] R. Cheacharoen, N. Rolston, D. Harwood, K.A. Bush, R.H. Dauskardt, M.D. McGehee, Design and understanding of encapsulated perovskite solar cells to withstand temperature cycling, Energy Environ. Sci. 11 (2018) 144–150, https://doi.org/10.1039/c7ee02564e.

[72] M.A. Green, General temperature dependence of solar cell performance and implications for device modelling, Prog. Photovoltaics Res. Appl. 11 (2003) 333–340, https://doi.org/10.1002/pip.496.

[73] R. Roesch, T. Faber, E. Von Hauff, T.M. Brown, M. Lira-Cantu, H. Hoppe, Procedures and practices for evaluating thin-film solar cell stability, Adv. Energy Mater. 5 (2015), https://doi.org/10.1002/aenm.201501407.

[74] P. Holzhey, M. Saliba, A full overview of international standards assessing the long-term stability of perovskite solar cells, J. Mater. Chem. A 6 (2018) 21794–21808, https://doi.org/10.1039/C8TA06950F.

[75] T. Nakada, M. Mizutani, 18% efficiency Cd-free Cu(In, Ga)Se2 thin-film solar cells fabricated using chemical bath deposition (CBD)-ZnS buffer layers, Jpn. J. Appl. Phys., Part 2 41 (2002) 97–100, https://doi.org/10.1143/JJAP.41.L165.

[76] Y.H. Khattak, F. Baig, S. Ullah, B. Marí, S. Beg, H. Ullah, Enhancement of the conversion efficiency of thin film kesterite solar cell, J. Renew. Sustain. Energy 10 (2018) 033501, https://doi.org/10.1063/1.5023478.